Experimental and Modeling Study of Electrochemical and Thermal Behavior of Lithium-ion Batteries

By

Soham Neupane
B.Tech. Jawaharlal Nehru Technological University Kakinada, 2014

Submitted to the graduate degree program in the Department of Mechanical Engineering and the Graduate Faculty of the University of Kansas in partial fulfillment of the requirements for the degree of Master of Science

_____
Dr. Xianglin Li, Chairperson

_____
Dr. Peter W. TenPas, Committee member

_____
Dr. Huazhen Fang, Committee member

Date defended _____

The Thesis Committee for Soham Neupane certifies that this is the approved version of the following thesis:

Experimental and Model Study of Electrochemical and Thermal Behavior of Lithium-ion Batteries

_____

Dr. Xianglin Li, Chairperson

Date approved: _____

Abstract

This research work starts with experimental investigations of the heat generation characteristics and the effectiveness of passive cooling of commercially available $LiFePO_4$ batteries (7.25mm×160mm×227mm, 19.5 Ah) using different cooling materials. The specific heat capacity and the entropy coefficient of the battery are experimentally measured. The heat generation rate of the battery at 1-4C current rates are also determined using three different methods: 1) the heat absorption calculated from the temperature increase of cooling water; 2) the energy loss calculated from the difference between the operating voltage and open circuit voltage and 3) the energy loss during a charge-discharge cycle calculated using the over-potential between charging and discharging. Results show that the heat generation rate estimated from heat absorbed by the water can be underestimated by up to 42.8% because of the temperature gradient within the battery and on the surface. The effectiveness of different passive cooling materials is compared at discharge current rates of 1-3C. The average increase of the battery surface temperature is 22.5, 17.1, 7.6, 7.2 and 6.3ºC at 3C using air, aluminum foam, octadecane, water with aluminum foam and water. Water, octadecane and water with aluminum foam could always maintain lower average temperature and temperature gradient on the battery surface.

In addition to that, this research also presents a simplified electrochemical-thermal coupled battery model to predict the electrochemical and thermal behavior of a lithium ion battery. The model predicts the current density distribution, electrolyte concentration, overpotential, temperature distribution and total heat generated by the battery at 1C, 2C and 3C current rates. The electrolyte concentration in the battery changes with the change in the applied current rate, which results in the change of the current density distribution throughout the electrodes. It is also observed that the internal resistance of the battery contributes significantly to the total heat generation and cannot be neglected. Higher increase in the battery surface temperature was observed using air as the cooling material compared to water. The model overpredicts the battery surface temperature by an average of 14.4% and 33.1% using air and the water as the cooling material because of the losses that occur during the experimental measurements.

Acknowledgements

It is a great pleasure to express my heartiest regards and deepest sense of gratitude to my advisor Dr. Xianglin Li for his esteemed supervision, inspiring advice, constant support, and enthusiastic encouragement during my time here. My grateful thanks are also extended to Dr. Peter W. TenPas and Dr. Huazhen Fang for serving on my committee.

The financial support provided by the Department of Mechanical Engineering is appreciated. I wish to thank all my lab mates for their contributions in providing valuable technical assistance and support during this research work.

Last but not the least, I would like to thank my parents, family, and friends for their constant support and encouragement throughout my study.

Contents

List of Figures

List of Tables

1. Introduction

A battery is an electrochemical device used for energy storage. They can be used to power electrical devices such as cellphones, computers, cars etc. Batteries store electrical energy in the form of chemical energy during charge and then convert the chemical energy back to electrical energy during discharge. There are two types of batteries available in the market: primary and secondary batteries. They are available in different shapes, sizes, and chemistries [1].

1.1 Types of battery

1.1.1 Primary batteries:

Primary batteries need to be discarded after complete discharge because the chemical reactions inside the primary batteries are not reversible. Primary batteries have high energy densities and commonly used in military and industrial systems [2]. They tend to lose 8 to 20% of their original charge every year at the room temperature. Primary batteries are usually small in size and are not suitable for heavy load applications.

1.1.2 Secondary batteries

The secondary batteries, also known as rechargeable batteries, can undergo multiple charging and discharging cycles with required power/current. The electrode compositions during discharging and charging cycle experience performance degradations due to the loss of active materials, loss of electrolyte, internal corrosions etc. after multiple charging and discharging cycles.

1.2 Battery shapes

Batteries are available in different shapes depending on their applications. Some of the most widely used battery shapes are:

1.2.1 Cylindrical cell

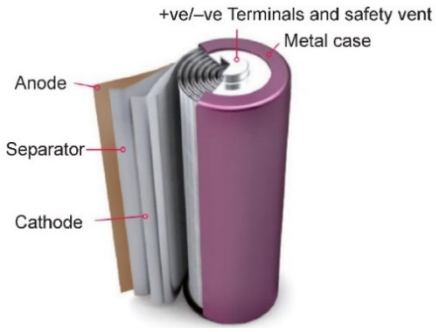

Figure 1.1: A cylindrical cell [4].

A cylindrical cell (Fig. 1.1) is the most widely used battery shape due to its good mechanical stability and easy manufacturing process. Most of these cells also contain pressure relief mechanism that is used as a safety feature in case of any unusual pressure build up inside the battery. Cylindrical cells offer long life and are economical though they are heavy and have less packing density. It is most widely used in power tools, medical instruments, laptop etc.

The size of cylindrical cells may vary depending on the application. They are numbered based on their size. The 18650 cylindrical cell is the most widely used and optimized cylindrical type of cell. The first two digits stand for the battery diameter in millimeters. The third and the fourth digit stand for the length in millimeters. The last digit zero is always there in all battery sizes. There are also some other commercially available cylindrical cell sizes like 20700, 21700, 22700, 26650 etc [3].

1.2.2 Button cell

Figure 1.2: Button/Coin cells [3].

Button cells (Fig. 1.2) also known as coin cells are small, compact design of batteries. These cells can also be stacked up into a tube to achieve higher voltages. Although small and inexpensive, it does not include any safety feature and has limited applications. Most of the button cells are non-rechargeable and are used mostly in wrist watches, hearing aids, car keys etc.

1.2.3 Prismatic cell

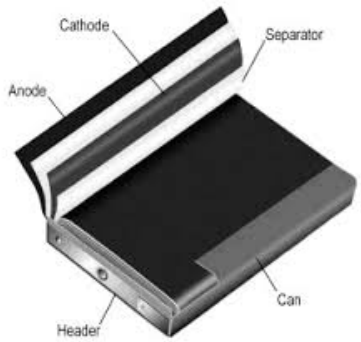

Figure 1.3: A prismatic cell [3].

Prismatic cells (Fig. 1.3) are thin battery cells with the optimal use of space. Each component is layered and wrapped in packages resembling a box. They are widely used in smartphones, tablets, laptops etc. Prismatic cells are expensive to manufacture, have a less efficient thermal management system and short cycle life. Various sizes of prismatic cells can be manufactured based on the application requirement.

1.2.4 Pouch cell

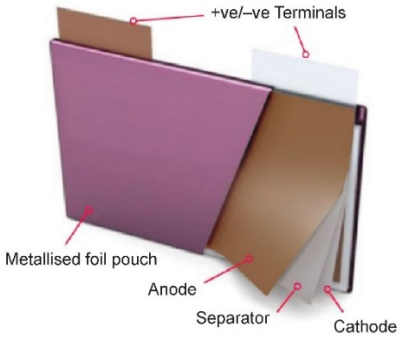

Figure 1.4: A pouch cell [4].

Pouch cells (Fig. 1.4) are flexible and lightweight battery design that has conductive tabs/terminals welded to the electrode available for external connections in a completely sealed way. There is some allowance kept in case swelling might occur. Pouch cells can deliver high current loads but perform best under light or moderate conditions. It makes the most use of space and has the best packaging efficiency of 90-95% among all battery shapes. Small pouch cells are used in drones etc. and large cells are used in energy storage systems and electric vehicles. Prismatic and pouch cells are being more widely used than cylindrical cells recently and the technology is moving towards the reduction of their manufacturing cost.

1.3 Battery chemicals

Battery chemicals i.e. the materials used for building the battery components play a crucial role in determining battery performance and safety. Different chemicals of primary and secondary batteries are available in the market. Extensive research works are being conducted on the study of various battery chemicals so as to find the optimal chemical for the majority of the applications.

Some of the popular chemicals of primary batteries are alkaline manganese, zinc carbon, zinc air, zinc manganese dioxide, lithium copper oxide, mercury oxide, lithium iron disulfide ($LiFeS_2$), lithium thionyl chloride ($LiSOCl_2$), lithium manganese dioxide ($LiMnO_2$) and lithium sulphur dioxide ($LiSO_2$), silver oxide etc. Some of the primary battery chemicals with their nominal voltages are listed in Table 1.1.

Table 1.1: Primary battery chemicals [5].

Chemistry	Nominal voltage (V)	Energy density (Wh/kg)
Zinc carbon	1.5	36.1
Zinc chloride	1.5	-
Alkaline zinc manganese dioxide	1.5	111.1-163.9
Zinc manganese dioxide/oxy nickel hydroxide	1.7	-
Zinc air	1.35-1.65	441.6
Silver oxide (silver zinc)	1.55	430.5
Lithium iron disulfide	1.5	-
Lithium manganese dioxide	3.0	230.5-280.5

Zinc carbon and zinc chloride are inexpensive chemicals. Zinc-chloride batteries have storage life up to 2 years [6]. Lithium chemicals are expensive but have longer shelf life than zinc chloride batteries and a lower rate of self-discharge. Lithium manganese dioxide batteries are the most popular chemistry with high energy density up to 280.5 Wh/kg and shelf life of about 10 years. They are also environment-friendly, leak proof and cost effective. The lithium iron disulfide is a relatively new chemistry and offers better performance than alkaline batteries with higher capacity and low internal resistance. It features better low-temperature performance, superior leakage resistance, lower self-discharge and storage life of 15 years [5]. The silver oxide cell is the most expensive chemistry [5], and are mostly used for heavy duty applications. Zinc air batteries are commonly used to power hearing aids. Silver oxide cells are used for button cells

applications. There are several unwanted hazards such as fire and explosion resulted by primary batteries due to the reaction between electrode and electrolytes, melting of lithium etc [7]. Hence, detailed studies of thermal behaviors and other properties of primary batteries are essential to create more efficient and safer batteries. Similarly, there are several chemicals of secondary batteries available in the market. Some of the chemicals along with their properties are listed in Table 1.2.

Table 1.2: Secondary battery chemicals.

Property	NiCd	NiMH	Lead-Acid	Li-ion	Li-ion polymer	Reusable Alkaline
Energy Density (Wh/kg)	45-80 [8]	60-120 [8,9]	30-50 [8]	90-250 [9,10]	100-130 [11]	80 [11]
Self-discharge/month (%)	15-20 [9]	20-30 [9,12]	5 [9]	5-10 [12]	10 [11]	0.3 [11]
Cycle Life (upto 80% of initial capacity)	1000 [9]	300-500 [9]	200-300 [9]	500-2000 [9]	300-500 [11]	50 [11]
Nominal Voltage (V)	1.25 [13]	1.25 [13]	2 [13]	3.6 [13]	3.6 [11]	1.5 [11]
Maximum discharge current rate	10C [10]	10C [10]	5C [10]	>30C [9,10]	>2C [11]	0.5C [11]
Operating temperature (^{o}C)	-40 to 60 [13]	-20 to 60 [13]	-20 to 60 [13]	-20 to 60 [13]	0 to 60 [11]	0 to 65 [11]
Coulumbic efficiency	70%-slow charge 90%-fast charge [11]		90% [11]	98% [15]	-	-
Cost per kWh ($)	400-800 [9]	250 [9]	150 [9]	300-2000 [9,14]	-	-

Secondary batteries have higher self-discharging tendency compared to primary batteries. Especially nickel based batteries self-discharge rapidly with a rate of 20-30% per month whereas modern lithium ion batteries have comparatively lower self-discharge rates of 5-10% per month. Lead-acid batteries are the oldest rechargeable batteries, and are still widely used in automobiles. However, it is not very environment-friendly because of the use of lead. Nickel metal hydride batteries were also extensively used in hybrid electric vehicles but they are being replaced by lithium ion batteries. Lithium ion batteries can achieve up to two times as high specific energy

and energy density [16] as nickel metal hydride batteries. Hence, lithium ion batteries show good scope in development of desired high power batteries with better safety for automotive application [17].

Lithium ion batteries provide longer life, better safety, and higher energy/power densities though they are slightly more expensive compared to other battery chemicals [18,19]. They are also called rocking chair battery or swing battery due to the two-way movements of lithium ion during charge and discharge process [1,16]. They require less maintenance compared to other battery chemicals. Despite being widely used in electric vehicles as well as portable electronics, lithium ion batteries are not yet advanced enough so as to perfectly meet every need for automotive applications. Different chemicals of lithium ion batteries are available for various applications. Some of the lithium ion chemicals along with their properties are listed in Table 1.3.

Table 1.3: Chemicals of lithium ion batteries.

Formula	Material	Energy density (Wh/kg)	Nominal Voltage (V)	Cycle life	Cost ($/kg)
$LiCoO_2$	Lithium Cobalt Oxide	150-250 [17]	3.7 [9]	500-1000 [18]	55 [19]
$LiMn_2O_4$	Lithium Manganese Oxide	100-150 [9]	3.8 [9]	500-1000 [22]	12 [19]
$LiNiCoAlO_2$	Lithium Nickel Cobalt Aluminum Oxide	100-150 [22]	3.7 [23]	2000-3000 [22]	35 [19]
$LiNiMnCoO_2$	Lithium Nickel Manganese Cobalt Oxide	100-170 [22]	3.7 [23]	2000-3000 [22]	33 [19]
$LiFePO_4$	Lithium Iron Phosphate	250 [9]	3.3 [9]	1000-2000 [18]	20 [19]
Li_2TiO_3	Lithium Titanate Oxide	60-75 [22]	2.4 [18]	3000-7000 [18]	-

Extensive works have been performed in order to find the best suitable lithium ion chemistry for automotive and other electronic application. Conventional $LiCoO_2$ batteries comprising of cobalt oxide cathode, graphite anode and electrolyte have an issue with the release of oxygen from the cathode at extreme conditions, which can react with the electrolyte during local

overheating and cause the thermal runaway [24]. On the other hand, Li_2TiO_3 batteries have a long cycle life of more than 5000 cycles, fast charging capability, wide temperature range, and better safety but are expensive to manufacture and have relatively low capacity. The $LiFePO_4$ batteries have flat discharge voltage, high power, and better safety [2,16,18,25]. Therefore, the $LiFePO_4$ batteries have emerged as one of the most promising batteries among all commercially available lithium batteries.

1.4 Battery terminologies

1.4.1 State of Charge

The state of charge (SoC) is the ratio of present charge of the battery and the total charge. It is expressed in percentage. 100% SoC means fully charged and 0% SoC means fully discharged.

1.4.2 Depth of Discharge

The depth of discharge (DoD) is the percentage of battery capacity that has been discharged with respect to the maximum capacity. It can be evaluated as:

$$DoD = (1- SoC) \quad (1.1)$$

1.4.3 Capacity

A battery's capacity is the amount of electric charge it can deliver at the rated voltage, which is the maximum voltage specified by the manufacturer beyond which a battery might show unexpected behaviors. It is measured in Ampere-hours (Ah). A battery of 20 Ah capacity can supply 20 A current for an hour at the ambient temperature. The capacity of a battery depends on the electrode material contained in it. The more active material in the electrodes leads to a higher battery capacity. The amount of stored charge that a battery can deliver depends on the battery chemical, current rates, required battery voltage, storage period, operating temperatures etc.

1.4.4 Current rate (C rate)

The current rate is a measure of the rate at which the battery is charged or discharged. It is defined as the applied charge/discharge current divided by the theoretical current drawn at which the battery would deliver its rated capacity in 1 hour. For example, for a battery of 20Ah, charging/discharging the battery using a current of 20 A, is equivalent to a 1C current rate. The charging/discharging process at 1C current rate takes 1 hour to reach the full battery capacity. Similarly, a 40 A current would be equivalent to 2C current rate that can charge/discharge a 20Ah battery in 30 minutes. It is better for a battery to discharge at a lower current rate in order to obtain a higher capacity. In addition, fast charging and discharging at high current rates

induces unwanted changes in the battery components such as heating issues, and capacity degradation that reduce the overall battery life.

1.4.5 Battery life

Battery life for non-rechargeable battery refers to the length of time a device can run on a fully charged battery. For rechargeable batteries, the battery life is the number of charge-discharge cycles that a battery can undergo without failing to meet its specific performance criteria [26]. The cycle life of a battery is greatly affected by the current rate, depth of cycles, operating temperature etc.

1.4.6 Self-discharge

Batteries tend to lose the original charge with time at different rates when stored for long periods. It is known as self-discharge and it occurs due to non-current-producing side chemical reactions occurring inside the cell. The rate of such side reactions reduces at lower temperatures.

1.4.7 Voltage

There are different types of voltage present in a battery cell. They are explained with the help of a plot presented in Fig. 1.5. In Fig. 1.5 (a) and (b), we can see the current density as a function of potential at the positive and the negative electrode during discharging and charging respectively. The current densities at the anode and the cathode is represented by i_a and i_c respectively. The absolute value of the current densities at each electrode is equal to the applied current density [27]. Different types of voltage related terms present in the battery are described below:

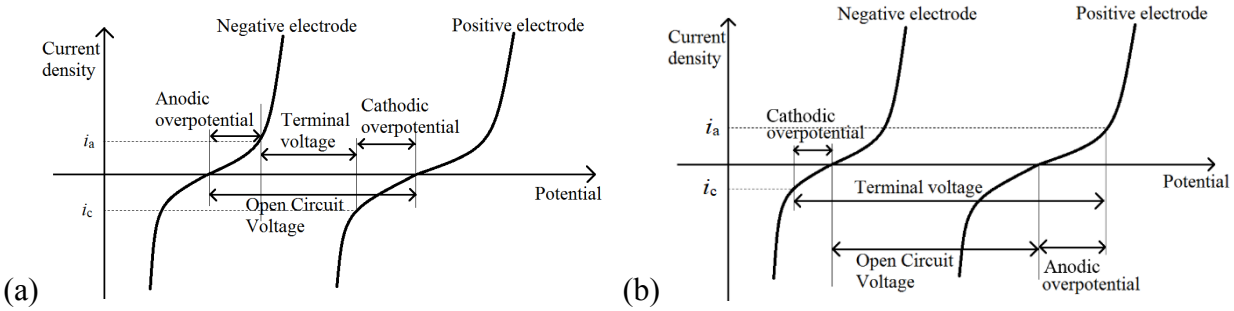

Figure 1.5: The (a) Discharge current density and (b) Charge current density as a function of electrode potential.

1.4.7.1 Terminal voltage and cut-off voltage

The difference between the potential of the two electrodes when the load is applied i.e. when there is some current applied to the battery is known as its terminal voltage as shown in Fig. 1.5.

The voltage across the battery terminals depends on the chemical reactions occurring inside the battery. A typical charge and discharge curve of a commercial 2.5Ah $LiFePO_4$ cell at C/6 current rate (±0.417 A) is shown in Fig. 1.6. The cell is charged from 2.5 V to the upper limit of 4.2 V. The discharge was then conducted until the lower limit of 2.5 V was reached. The safe voltage limits (2.5 V and 4.2 V in Fig. 1.6) selected to stop the charging and discharging process is known as the cut-off voltage of the battery.

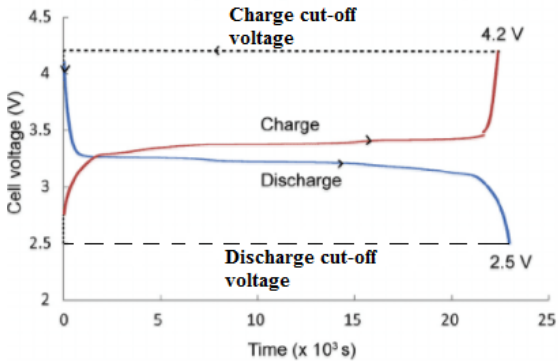

Figure 1.6: Charge and discharge curves of a commercial LiFePO4 cell [28].

1.4.7.2 Open Circuit Voltage

The voltage of a battery when it's not connected to any external source (i.e. when no current is applied to the system) is called the open circuit voltage (OCV) of the battery. We can tell from the Fig. 1.5 (a) and (b) that the OCV of the battery is always larger than its terminal voltage while discharging. The positive electrode is polarized negatively giving a negative cathodic current density and the negative electrode is polarized positively giving a positive anodic current density during discharging resulting in a lower terminal voltage than the OCV [29]. Whereas during charging, the negative electrode is polarized negatively resulting in negative current, and the positive electrode is polarized positively to generate positive current. This results in a higher terminal voltage compared to the OCV during the charging process [29].

1.4.7.3 Overpotential

Overpotential is defined as the difference between the potential of the electrode with and without current [27]. In other words, overpotential is the potential difference between the theoretical voltage and the actual voltage under operating conditions. Both anode and cathode have their own overpotential values and are termed as anodic overpotential and cathodic overpotential, respectively.

1.5 Working mechanism

A $LiFePO_4$ battery cell is used as an example (Fig. 1.7) to understand the working mechanism of a lithium-based rechargeable battery. The reactions taking place inside the battery electrodes of $LiFePO_4$ battery half-cells are as follows:

$$\text{Negative electrode: } Li_xC_6 \underset{\text{charge}}{\overset{\text{discharge}}{\rightleftharpoons}} Li_{x-z}C_6 + z\,Li^+ + z\,e^- \tag{1.2}$$

$$\text{Positive electrode: } Li_yFePO_4 \underset{\text{discharge}}{\overset{\text{charge}}{\rightleftharpoons}} Li_{y-z}FePO_4 + z\,Li^+ + z\,e^- \tag{1.3}$$

Where x is the number of moles of lithium present in the graphite/carbon (C_6) structure, y is the number of moles of lithium present in the iron phosphate ($FePO_4$), z is the number of moles of lithium taking part in the electrochemical reaction and Li^+ is the lithium ion. The 4 major components of a lithium ion battery are: the cathode electrode, the anode electrode, the electrolyte, and the separator, which are discussed in detail below.

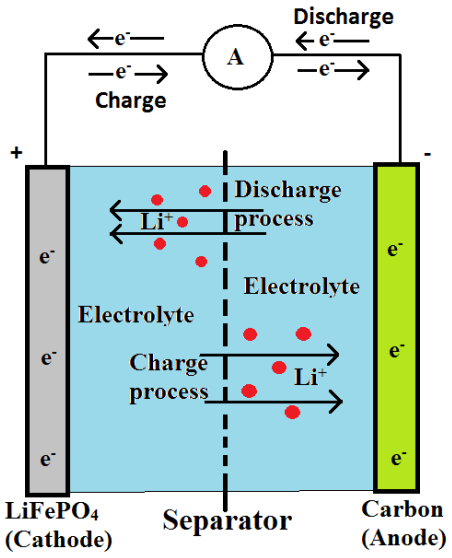

Figure 1.7: The schematic illustration of a $LiFePO_4$ battery.

1.5.1 Cathode

The cathode is the positive electrode of a battery that is made of lithium composite ($LiFePO_4$). It emits lithium ion to the anode during charging and receives lithium ion during discharging. The cathode is made up of porous material to obtain better cycle life, capacity, and current rate application compared to the bulk non-porous materials. A porous electrode may

comprise of a single reactive electronic conductor or a mixture of two solids [30]. Some of the commercially available cathode materials for a lithium ion batteries are listed in Table 1.3.

1.5.2 Anode

The anode is the negative electrode of a battery made of graphite powder (carbon). It receives lithium ion from anode during charging and emits lithium ion during discharging. The anode is also made of a porous material for the similar reason as the cathode. There are mostly 2 types of commercially available anode materials, which are graphite/carbon and lithium titanate oxide ($Li_4Ti_5O_{12}$) [31]. Graphite is abundant and has longer cycle life but can only provide low energy density (37.2 Wh/kg). Lithium titanate oxide has better efficiency, higher voltage, and higher energy density (262.5 Wh/kg).

1.5.3 Electrolyte

The electrolyte can be solid, liquid or polymer depending on the type of battery. Solid electrolytes are mostly used with gaseous or liquid electrodes. Polymer electrolytes are used instead of solid electrolytes where good electrode-electrolyte contact cannot be achieved using a solid state electrolyte [32]. Liquid electrolytes are common in portable electronic applications since they offer high electrochemical stability, high voltage and excellent energy density [33]. The electrolyte used in lithium ion batteries is typically made from lithium salts dissolved in a mixture of organic solvents [33]. The electrolyte is present throughout the space between anode and cathode to conduct lithium ions between the two electrodes. Due to the lower ionic conductivity of the electrolyte compared to the electronic conductivity of the electrodes, a thin layer (~25 μm) of electrolyte is typically applied in the battery to reduce the ohmic resistance.

1.5.4 Separator

A separator is a micro-porous membrane present in between the anode and cathode electrodes to prevent short circuit and to allow the flow of lithium ion only through the electrolyte that saturates the separator. The separator also helps in preventing mixing of electrolytes if two different electrolytes are used in a battery [34]. A separator needs to absorb and retain a significant amount of electrolyte to achieve low internal resistance and high ionic conductivity. It must be chemically and electrochemically stable to electrodes and electrolytes, and does not produce any unwanted materials. Moreover, it should also be able to withstand corrosive nature of the electrolyte at higher temperatures [35]. Separators are generally made of non-woven fibers (cotton, nylon), polymer films (polyethylene (PE), polypropylene (PP)),

ceramic etc [36,37]. Some of the commercially available separators are Celgrad 2324, Celgrad 2340, Tonen-1 and Tonen-2. Tonen-1 and Tonen-2 are made of PE whereas Celgrad 2325, and Celgrad 2340 are made up PP-PE-PP chain. The thicknesses of the commercially available Celgrad 2325, Celgrad 2340, Tonen-1, and Tonen-2 are 25 μm, 38 μm, 25 μm, and 30 μm respectively.

As seen in Fig. 1.7, each battery consists of two half cells connected in series by the electrolyte. One-half comprises of negative electrode (anode) filled with electrolyte and the other half comprises of positive electrode (cathode) filled with electrolyte. Anode acts as the negative electrode, and cathode acts as the positive electrode during discharge and vice versa. In lithium ion batteries, lithium ions move between the anode and cathode. When connected to an external device, the movement of electrons occur and complete the chemical reaction so as to deliver energy. This results in a flow of electron through the external connection, which provides power. In the discharging process, the lithium ion in the anode (carbon) is ionized and dissolved into the electrolyte. Then, the lithium ions move through the separator and insert into atomic size holes in the cathode ($LiFePO_4$). The anode is the source of the electron from where they flow through the external connection to the cathode. Since this process is reversible, current is carried by lithium ions from the positive electrode (cathode) to the negative electrode (anode) during charging [38]. The lithium ions are small and lie within the electrode materials without causing any sort of harm to the battery [39]. Each half cell has their own potential and the net potential of the cell is the difference between the potential of two half cells.

1.6 Research focus

Although lithium ion batteries are a promising energy storage technologies because of their stability, high energy density, safety etc. for future electrification of vehicles, there are plenty of spaces left for improvements [2,18]. Several accidents have been reported over time due to lithium ion battery hazards, thus, raising concerns on commercializing them in automobile industry [40,41]. Some of the major problems associated with commercializing lithium ion batteries in electric vehicles are their safety, cost and temperature issues which are all somehow related to the thermal effect of the battery [32,42].

During charging/discharging cycles, changes in the electrode volume, electrode-electrolyte reactions and electrode decomposition occur that can result in capacity loss [42]. Researchers are working on the use of advanced materials such as nano-particles etc. for the anode, cathode, and

electrolytes in order to further improve the energy, power, cost, reliability, time and safety factor of a lithium ion battery [1,17,25,43-45]. The temperature of a battery also plays an important role in its capacity fade and power degradation due to loss of active material and impedance rise respectively [42,46,47]. Battery over discharging leads to the reduction of electrolyte that results in the production of combustible gas and thus poses potential hazards. Similarly, overcharging will cause the positive electrode to decompose and produce high heat leading to unwanted hazards [43]. The safe operating temperature for most of the batteries, in general, would be -20^{o}C to 55^{o}C for discharging and 0 to 45^{o}C for charging [48]. Above the safe temperature limit, the exothermic reaction between electrodes and electrolyte come into play that can raise the internal temperature of a battery abnormally [41].

Without a proper thermal management even local heat spots generated in a battery can pose a serious hazard. Thus, the proper thermal management of a battery is one of the major concerns in the field of battery research since it plays a crucial role in improving battery performance as well as safety. This work focuses on the experimental determination of battery heat generation characteristics at high current rates up to 4C, comparison of different heat generation estimation methods and comparative study of the effectiveness of several passive cooling materials. These studies are all crucial for designing of a proper thermal management system. The battery used for the experimental study is a commercially available 19.5Ah $LiFePO_4$ with the size of 7.25 mm×160 mm×227 mm provided by Smith Electric Vehicles (located in Kansas city). In addition to that, this study also presents a simplified electrochemical-thermal coupled model of a battery that can be used for simulating the electrochemical as well as the thermal behavior of a battery. The temperature distributions within the battery components, at the battery surface as well as within the cooling material surrounding the battery can be estimated using this model. Detailed estimation of temperature can be used for proper heat generation estimation by the battery at different current rates.

Nomenclature

SoC	State of Charge
DoD	Depth of Discharge
OCV	Open Circuit Voltage
C rate	Current rate

References:

[1] M. Wakihara, Recent developments in lithium ion batteries, Materials Science and Engineering. R33 (2001) 109-134.

[2] B. Dunn, H. Kamath, J. Tarascon, Electrical Energy Storage for the Grid: A Battery of Choices, Materials For Grid Energy. 334(2011) 928-935.

[3] http://batteryuniversity.com/learn/article/types_of_battery_cells

[4] P. Millers, State of the art and future developments in lithium-ion battery packs for passenger car application, Johnson Matthey Technological Review. 59 (2015) 4-13.

[5] http://www.epectec.com/batteries/chemistry/

[6] http://support.radioshack.com/support_tutorials/batteries/bt-zicl-main.htm

[7] D. Lisbona, T. Snee, A review of hazards associated with primary lithium and lithium-ion batteries, Process Safety and Environmental Protection. 89 (2011) 434-442.

[8] http://www.epectec.com/batteries/cell-comparison.html

[9] A. Chen, P.K. Sen, Advancement in Battery Technology: A State-of-the-Art Review, Institute of Electrical and Electronics Engineer. (2016-ESC-0713) 1-10.

[10] A. Scott, Challenging Lithium-Ion Batteries with New Chemistry, Chemical & Engineering News. 90 (2015) 18-19.

[11] http://batteryuniversity.com/learn/article/secondary_batteries

[12] Characteristics of Rechargeable Batteries, Texas Instruments (2015).

[13] http://batteryuniversity.com/learn/archive/whats_the_best_battery

[14] Y. He, Y. Wang, H. Li, X. Huang, Alumina-Coated Patterned Amorphous Silicon as the Anode for a Lithium-Ion Battery with High Coulombic Efficiency, Advanced Materials. 23 (2011) 4938-4941.

[15] M. Lowe, S. Tokuoka, T. Trigg, G. Gereffi, Lithium-ion Batteries for Electric Vehicles: THE U.S. VALUE CHAIN, Environmental Defense Fund. (2010) 1-76.

[16] Z. Li, D. Zhang, F. Yang, Developments of lithium-ion batteries and challenges of LiFePO4 as one promising cathode material, Journal of Material Science. 44(2009) 2435-3316.

[17] S. Megahed, B. Scrosati, Lithium-ion rechargeable batteries, Journal of Power Sources, 41(1994) 79-104.

[18] http://batteryuniversity.com/learn/article/bu_216_summary_table_of_lithium_based_batteries

[19] E.J. Berg, C. Villevieille, D. Streich, S. Trabesinger, P. Novak, Rechargeable Batteries: Grasping for the Limits of Chemistry, Journal of The Electrochemical Society. 14 (2015) A2468-A2475.

[20] K. Onda, T. Oshima, M. Nakayama, K. Fukuda, T. Araki, Thermal behavior of small lithium-ion battery during rapid charge and discharge cycles, Journal of Power Sources. 158 (2006) 535-542.

[21] A. Optiz, P. Badami, L. Shen, K. Vignarooban, A.M. Kannan, Can Li-Ion batteries be the panacea for automotive applications?, Renewable and Sustainable Energy Reviews. 68 (2017) 685-692.

[22] A. Stan, M. Swierczynski, D. Stroe, R. Teodorescu, S. J. Andreasen, Lithium Ion Battery Chemistries from Renewable Energy Storage to Automotive and Back-up Power Application- An Overview, IEEE. 14 (2014) 713-720.

[23] N. Nitta, F. Wu, J.T. Lee, G. Yushin, Li-ion battery materials: present and future, materialstoday, 18(2015) 252-264.

[24] B. Scrosati, J. Hassoun, Y. Sun, Lithium-ion batteries. A look into the future, Energy and Environmental Science. 4 (2011) 3287-3295.

[25] X. Zhou, F. Wang, Y. Zhu, Z. Liu, Graphene modifies LiFePO4 cathode materials for high power lithium ion batteries, Journal of Materials Chemistry, 21(2011) 3353-3358.

[26] A Guide to Understanding Battery Specifications, MIT Electric Vehicle Team (2008).

[27] https://www.comsol.com/blogs/does-the-current-flow-backwards-inside-a-battery/

[28] S. Ramdon, B. Bhushan, S.C. Nagpure, In situ electrochemical studies of lithium-ion battery cathodes using atomic force microscopy, Journal of Power Sources. 249 (2014) 373-384.

[29] https://www.comsol.com/blogs/does-the-current-flow-backwards-inside-a-battery/

[30] J. Newman, W. Tidemann, Porous-Electrode Theory with Battery Applications, American Institute of Chemical Engineers. 21 (1975) 25-41.

[31] K.C. Kam, M.M. Doeff, Electrode Materials for Lithium Ion Batteries, Material Matters. V7 (2012).

[32] J. B. Goodenough, K. Park, The Li-Ion Rechargeable Battery: A Perspective, Journal of The American Chemical Society. 135 (2013) 1167-1176.

[33] Q. Li, J. Chen, L. Fan, X. Kong, Y. Lu, Progress in electrolytes for rechargeable Li-based batteries and beyond, Green Energy & Environment. 1 (2016) 18-42.

[34] L. Yuan, Z. Wang, X. Hu, J. Chen, Y. Huang, J. B. Goodenough, Development and challenges of LiFePO4 cathode material for lithium-ion batteries, Energy & Environmental Science. 4(2011) 269-284.

[35] H. Lee, M. Yanilmaz, O. Toprakci, K. Fu, X. Zhang, A review of recent developments in memberance separators for rechargeable lithium-ion batteries, Energy & Environmental Science, 7(2014) 3857-3886.

[36] http://www.targray.com/li-ion-battery/separators/ceramic-separators

[37] S.S. Zhang, A review on the separators of liquid electrolyte Li-ion batteries, Journal of Power Sources. 164 (2007) 351-364.

[38] Costs of Lithium-Ion Batteries for vehicles, Center of Transportation Research, Argonne National Laboratory, United States Department of Energy.

[39] M. M. Thackeray, C. Wolverton, E. D. Isaacs, Electrical energy storage for transportation-approaching the limits of, and going beyond, lithium-ion batteries, Energy & Environmental Science. 5(2012) 7852-7863

[40] Q. Wang, P. Ping, X. Zhao, G. Chu, J. Sun, C. Chen, Thermal runaway caused fire and explosion of lithium ion battery, Journal of Power Sources. 208 (2012) 210-224.

[41] P.G. Balakrishnan, R. Ramesh, T. P. Kumar, Safety mechanisms in lithium-ion batteries, Journal of Power Sources. 155 (2006) 401-414.

[42] T. M. Bandhauer, S. Garimella, T. F. Fuller, A Critical Review of Thermal Issues in Lithium-Ion Batteries, Journal of The Electrochemical Society, 158(2011) R1-R25

[43] B. Scrosati, J. Garche, Lithium batteries: Status, prospects and future, Journal of Power Sources. 195 (2010) 2419-2430.

[44] J.M. Tarascon, M. Armand, Issues and challenges facing rechargeable lithium batteries, Nature. 414 (2001) 359-367.

[45] H. Li, Z. Wang, L. Chen, X. Huang, Research on Advanced Material for Li-ion Batteries, Advanced Materials. 21(2009) 4593-4607.

[46] A. Barre, B. Deguilhem, S. Grolleau, M. Gerard, F. Suard, D. Riu, A review on lithium-ion battery ageing mechanisms and estimations for automotive applications, Journal of Power Sources. 241 (2013) 680-689.

[47] J. Vetter, P. Novak, M.R. Wagner, C. Veit, K.C. Moller, J.O. Besenhard, M. Winter, M. Wohlfahrt-Mehrens, C. Vogler, A. Hammouche, Ageing mechanisms in lithium-ion batteries, Journal of Power Sources. 147 (2005) 269-281.

[48] L. Lu, X. Han, J. Li, J. Hua, M. Ouyang, A review on the key issues for lithium-ion battery management in electric vehicles, Journal of Power Sources. 226 (2013) 272-288.

2. Experiment

2.1 Literature review

Present energy sources that are mainly based on burning fuels pose a serious concern about carbon dioxide emission related issues that cause global warming [1-3]. Fossil fuels are non-renewable energy source and are likely to come to an end in near future [3]. Hence, efforts are aimed at ensuring proper use of renewable sources to replace internal combustion engines with electric motors for sustainable use. Among all the possible choices, the most suitable source of power as well as energy storage is batteries [2]. Thus, most research works on lithium ion batteries are directed towards commercializing their use in the automobile industry.

Electro-vehicular application of batteries requires them to undergo charging and discharging process at very high current rates for long periods. This results in high heat generation and temperature increase within the battery and on its surface. The elevated temperatures during the charging and discharging have detrimental effects on battery life and efficiency. It may even lead to unwanted fire hazards [4,5]. Battery hazards such as explosion or fire in addition to leakage or irreversible damage may happen due to several misuse or malfunction such as overcharging, use of very high current rates, short circuit etc. Car batteries are most likely to explode when a short circuit generates very large currents.

Thermal stability of a battery depends on the amount of heat it can dissipate. Effective heat dissipation is required in both cell and pack level. Some studies have experimentally measured the basic important thermal properties such as specific heat, entropic heat coefficient of certain types of lithium-ion batteries in order to estimate the heat generation [6-11]. The specific heat capacity plays an important role to determine the temperature increase in a cell with a given amount of heat generation [7-13]. Similarly, the rate of entropy change with temperature, which depends on the battery chemistry and temperature, is also crucial to determine the reversible heat generation rate.

Lin et. al [7] characterized the heat generation of a prismatic battery cell using an accelerated rate calorimeter. The heat generated by the battery was calculated using the measured specific heat capacity and temperature increase data. Specific heat capacity was measured using an assembly where the heater with a constant heat flux was sandwiched between two cells placed into an adiabatic chamber. The specific heat of the battery was determined to be 1067 J kg^{-1} K^{-1}. The battery changed from an endothermic state initially to an exothermic state when it was

charged and discharged at the current rate of 0.33C due to the effect of the reversible heat. The trend of heat generation at 1C and 2C current rates during discharging also showed endothermic followed by exothermic thermal behavior. Charging at 1C and 2C current rates, however, did not exhibit the endothermic behavior. They concluded that, even for well-designed large batteries, Joule heating in the current collectors is higher than reversible heat. It was seen that the trends of heat generation rate during both charging and discharging were nonlinear and S-shaped. To determine the reversible heat rate, the entropy coefficient was determined by measuring the open circuit voltage (OCV) values at different temperatures. The entropy coefficients changed from negative to positive at SoC of 0.4.

Bandhauer et al [9] also calculated the reversible heat generation using the entropy coefficient. It was determined from the slope of OCV with temperature (with the temperature range of 15–55°C) at a required SoC. The irreversible heat generation rate was evaluated using the cell over-potential. The heat generation rate increased with an increase in current rate. The entropy coefficients were found to be within the range of ±9.93 μV K^{-1} and ±13.43 μV K^{-1} for the two battery samples they tested. They concluded that the heat generation rate is a strong function of ambient temperature between 15°C and 5 °C, especially at high current rates because both transport properties and kinetics are functions of temperature in lithium-ion batteries. At low temperature, the irreversible heat increased with the decrease of temperature due to mass transport and kinetic limitations, whereas the reversible potential is not a strong function of temperature.

Chen et al. [14] investigated the heat generation rate as well as the efficiency of 20-Ah $LiFePO_4$ lithium-ion pouch cell at different temperatures (-10–40°C). The battery was sandwiched between two high-density polyethylene plates 4 times thicker than the battery. A 10-W heater was used to calibrate the calorimeter. They illustrated that the heat generation increased with the increase of the discharge current rate. At low discharge current rate (0.25C), the heat was endothermic. The heat generation was found to decrease with the increase in temperature due to the increased rates of mass transport and reduced activation loss which reduced over-potential during discharge. They also showed that the battery capacity increased with the increase of the temperature due to the higher ionic conductivity at higher temperature. The preferred operating temperature of the prismatic lithium-ion battery was between 30°C and 40°C.

Chen et al. [15] studied the effect of several passive cooling materials on lithium-ion battery performance. They compared the performance of air with the mixture of water and ethylene glycol (50-50 vol). The battery capacity decreased by 0.95% when the ambient temperature was lowered from 20°C to -10°C due to decrease in ionic conductivity and slowdown of electrochemical reactions of the battery. The optimum operating temperature was found to be around 20°C to 30°C, where the capacity of the battery was near the maximum and the performance degradation was minimized. A comparison between the battery capacity using water-ethylene glycol and air at 20°C showed that though the water ethylene glycol mixture helped in maintaining lower battery surface temperature, higher capacity was obtained when the battery was cooled by air because of higher temperature of the air-cooled battery.

Alipanah et al. [16] numerically studied passive thermal management systems of lithium-ion batteries made from pure octadecane, pure gallium and octadecane-aluminum foam composite materials at different heat fluxes and metal foam porosities. They concluded that convective heat transfer was one of the most important factors affecting the battery surface temperature uniformity.

Many studies [6-11,17] reported in literature are based on cylindrical or prismatic cells. We know that pouch cells have better compactness and packing efficiency compared to other type of cells (cylindrical cell, coin cell, and prismatic cell) and are widely used in vehicular operations. Hence, higher capacity pouch cells have also been an interest of study. In the case of high capacity cells, many experimental studies are limited to a maximum current density of 2C, which might not be enough for high power applications during acceleration and fast charging of electric vehicles.

The approach towards estimating the heat generation rate of a battery is also very important. Heat generation estimation using different methods could vary significantly based on the accuracy of experimental approaches, errors and uncertainties of measurements, and accuracies of used instruments. Thus, proper comparison of different approaches and identification of the most accurate method to predict the heat generation during charging/discharging cycles at high current rates is essential. Various heat generation estimation methods are comparatively studied as an important objective of this work.

This study also investigates the entropy coefficient and heat capacity of a pouch cell. Moreover, this work also includes a comparative study of 5 different passive cooling materials

on batteries, which are crucial to maintaining proper operating temperature and low temperature gradients without significantly increasing the weight, volume, and cost of the battery system. The obtained data and information are important for designing the thermal management systems for batteries and also to build accurate battery models and estimate the heat generation and temperature increase of lithium-ion batteries with better understanding.

2.2 Experimental Apparatus and Procedure

2.2.1 Measurements of the entropy coefficient

The experimental setup comprises of battery cycling equipment (Arbin Instrument MSTAT4) and a temperature controlled water bath (Fisher Scientific's Isotemp 4100H7). The computer managed Arbin software for measurement of charging/discharging current, charging/discharging energy and charging/discharging capacity, maximum/ minimum voltage and voltage at each time point. The battery cycling equipment could be programmed to charge and discharge a battery cell at constant current rates from 1 A to 5 A or at constant voltage as per the requirement. The water bath was set up to maintain the constant water temperature ranging from 5 °C to 85 °C for the desired time interval.

A commercially available $LiFePO_4$ pouch cell of 19.5 Ah capacity provided by Smith Electric Vehicles was kept inside the water bath with the active area completely immersed in water and only the electrode outside the water surface in order to avoid short circuit and maintain required uniform temperature on the battery surface throughout the experiment. The battery has the dimension of (7.25× 160 ×227) mm^3, active area of (7.25×152.4×203.2) mm^3, nominal voltage of 3.3V, and energy density of 247 Wh/L.

Battery's cut-off voltage for discharging and charging was set to be 2.5 V and 3.7 V, respectively. The cut-off voltages were determined by running the cell for a full charging and discharging cycle at a very low current of 1A (0.05C). The battery was charged and discharged with a current rate of 5 A (0.25C) to the SoC of 0.0, 0.1, 0.2, 0.4, 0.6, 0.8 and 1.0 in the abovementioned voltage range. At each SoC, the battery was allowed to rest in the water bath for 30 minutes and the OCV of the battery was measured every 10 seconds using the Arbin battery tester. The temperature of the water bath for the test was maintained at 20°C, 25°C, 30°C, 35°C, 40°C, 45°C and 50°C respectively. The battery was then allowed to rest under room temperature for at least 5 hours after the temperature cycle. The battery was then charged to the next SOC and the same procedure was repeated. All the tests have been repeated at least three times.

Entropy coefficient, which is the change of OCV with temperature, was calculated and averaged at various temperature points:

$$\frac{\partial OCV}{\partial T} = \frac{1}{n}\sum_{i=1}^{n-1} \frac{\mathrm{OCV}_{i+1} - \mathrm{OCV}_i}{T_{i+1} - T_i} \quad (1.1)$$

Where $\partial \mathrm{OCV}/\partial T$ is the entropy coefficient, T is the temperature and n is the number of temperature points in which the experiment was performed.

2.2.2 Measurement of the specific heat capacity

The experimental setup for specific heat capacity measurement of the battery comprised of a silicon heater (Omega SRFG-608/2) sandwiched between two battery cells enclosed in an acrylic container with the specific heat of 1470 J/kg/K and density of 1150 kg/m^3. The heat radiated by the heater on both sides was observed using a FLIR A300 thermal camera (model 48201-1001). The thermal camera could produce the thermal image of an object with details of the temperature along its surface. Hence, the equal amount of heat radiated from both sides of the heater could be observed during the operation.

The rectangular enclosure with inside volume of 240×155×22 mm^3 was made of acrylic sheets (Makrolon polycarbonate manufactured by BAYER) of thickness 12.5 mm. A 3 mm width groove with 4 mm depth was cut off on the mid-width of the side and bottom walls in order to place the battery in the middle of the container to minimize the heat loss through the container. The enclosure was covered by foam rubber insulation to reduce the heat loss to the surroundings during experiments. T-type thermocouples (Omega Engineering Inc., USA) were used to measure temperature inside the container and on the battery surface. Three thermocouples were attached on each side of the battery. One thermocouple was inserted through a small hole drilled on each side of the container to measure the temperature and estimate the heat loss through the container. One thermocouple was also used to record the temperature of the air inside the container to account for heat absorbed by the air.

Temperature data was recorded at 1-minute time intervals using KEYSIGHT 34972A LXI Data Acquisition/Switch Unit. A digital weighing scale NV4101 manufactured by OHAUS was used to measure the weight of the batteries and the container. Also a DC power-supplying device GPR-30H10D manufactured by GWINSTEK provided constant power to the heater to generate uniform heat flux until the temperature of the battery surface reached 60ºC. Using the temperature data at the battery surface, temperature of the air inside the container, as well as

temperatures of the container walls, the specific heat capacity of the battery is evaluated based on the energy balance using eq (1.2):

$$Q = (mc_p\mathrm{d}T)_{\text{battery}} + (mc_p\mathrm{d}T)_{\text{walls}} + (mc_p\mathrm{d}T)_{\text{insulation}} + (mc_p\mathrm{d}T)_{\text{air gap}} \quad (1.2)$$

It is also estimated that the amount of heat absorbed/lost through the insulation was negligible compared to the heat absorbed by the battery and container.

2.2.3 Heat generation measurement

Fig. 2.1 shows the experimental setup used to study the heat characteristic and passive cooling of lithium-ion batteries using different materials. The experimental setup consisted of five parts: a rectangular enclosure with the cooling material, a data acquisitions system, a lithium-ion battery, a battery discharger (BK PRECISION-8150), and a TDK-Lambda battery charger (UPS-132). The thickness of the battery is 7 mm and the space between the battery and wall at each side has a width of 7.5 mm.

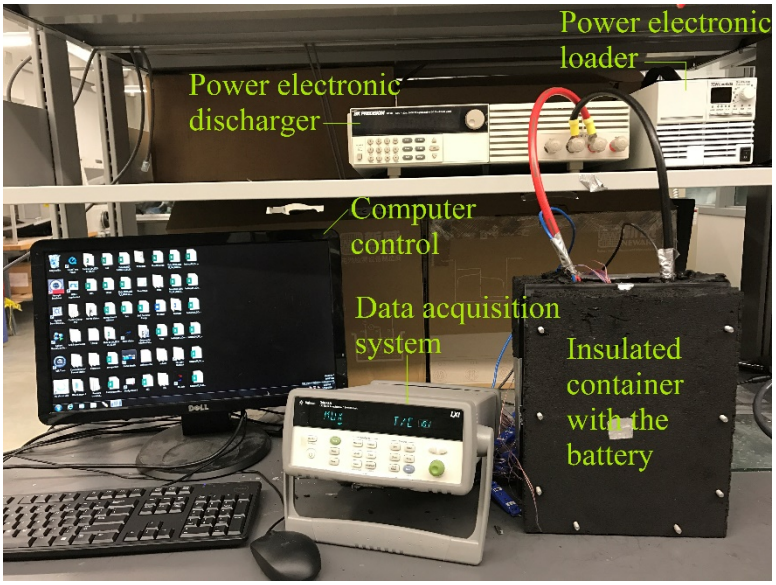

Figure 2.1: The experimental setup for heat generation measurement.

A total of 13 T-type thermocouples (Omega Engineering Inc., USA) with an accuracy of ±0.5ºC were used to record the temperature change. Five of those thermocouples were used to track the battery surface temperatures (Fig.2.2) and the rest were used to track the temperature of cooling material, container walls, air gap in the container and ambient temperature of the laboratory.

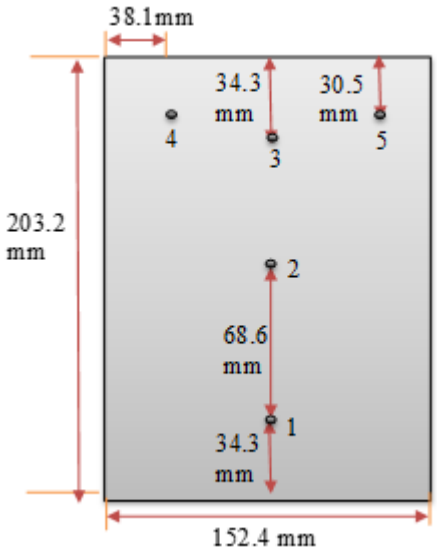

Figure 2.2: Thermocouple locations on the battery under heat generation test.

Temperatures measured by the thermocouples were recorded every 20 s by a KEYSIGHT 34972A data acquisition/switch unit. Before the start of the experiment, the setup was placed in the laboratory overnight to reach a uniform atmospheric temperature throughout the battery. Discharge and charge tests of batteries at given current rates (1, 2, 3, and 4C) were conducted. The following procedures were repeated for each test:

Discharging:

a) Pretest: Charge the battery cell with 2.5 A current and 3.9 V cut-off voltage.
b) Rest the battery for at least 5 h at environmental temperature.
c) Discharge the battery from 0.0 to 0.8 SoC at a constant current rate.
d) Repeat the above procedure at least three times at each current rate.

Charging:

a) Pretest: Discharge the battery cell with 2.5 A current and 2.5 V lower cut-off voltage.
b) Rest the battery for at least 5h at environmental temperature.
c) Charge the battery from 0.0 to 0.8 SoC at a constant current rate.
d) Repeating the above procedure at least three times at each current rate.

The experimental error of the heat generation test was determined using a flexible heater (Omega SRFG—608/2). The calibration tests were performed using two flexible heater outputs of 600 W/m^2 attached on the front and back sides of the battery. The test was performed until the maximum battery surface temperature reached 60°C. The test was repeated three times and the

temperatures were recorded. Using equation (1.2), the heat absorbed by the setup was determined. It was seen that the obtained value of heat absorption was in 90% agreement with the actual heat supplied by the heater and the remaining 10% was due to some instrumental error and heat lost to the atmosphere through natural convection.

2.3 Results and Discussion

2.3.1 Measurement of voltage and the entropy coefficient

The OCV of the battery cell is measured at various SoC and temperature. OCV has almost linear relations with temperature at 0.0, 0.2, 0.4 and 0.6 SoC whereas non-linear behavior was observed at 0.8 and 1.0 SoC [7,12]. The slopes of OCV with respect to temperature were used to find the entropy coefficient as given in eq (1.1). The calculated entropy coefficients as a function of SoC are shown in Fig. 2.3.

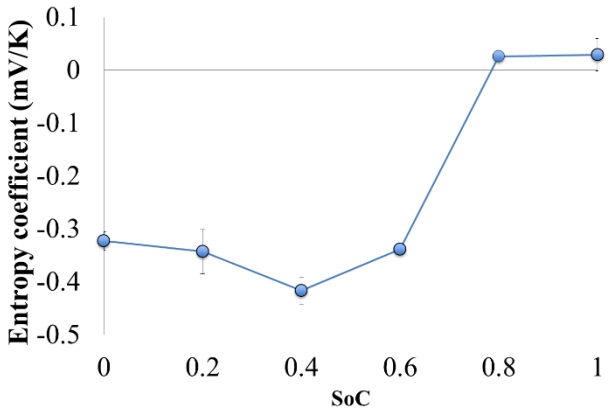

Figure 2.3: The entropy coefficient (mV/K) of the battery as a function of SoC.

As shown in Fig.2.3, the entropy coefficient is negative when the SoC is low and positive when SoC was 0.8 and above. The least and highest value of the entropy coefficient is obtained as -0.416 mV/K to 0.029 mV/K at 0.4 SoC and 1 SoC respectively. The entropy coefficients at different SoCs are of the similar magnitude as reported in other studies and also exhibit similar trends [7-9,12].

2.3.2 Specific heat capacity measurement

Constant heat fluxes of 30 W, 40 W and 50 W were supplied through the heater until the temperature of the battery surface reached 60°C. Eq (1.2) was used to calculate the specific heat capacity of the battery. The average of the heat capacities obtained at 30 W, 40 W and 50 W power flux resulted to an average specific heat capacity of the battery as 932.5±78 J/kg/K. The

obtained value of specific heat capacity is close with the value reported in previous studies for a battery of the same chemistry but different capacity [7].

2.3.3 Heat generation measurement

2.3.3.1 Charging vs discharging

The heat generation rates measured and estimated using temperature increase approach between charge and discharge of the battery at the current rates of 1, 2, 3 and 4C current rates as a function of SoC and depth of discharge (DoD) ranging from 0.0 to 0.8 in steps of 0.1 are shown in Fig.2.4. The heat generation rates of the battery in both charge and discharge increase with increasing SoC during charge and DoD during discharge.

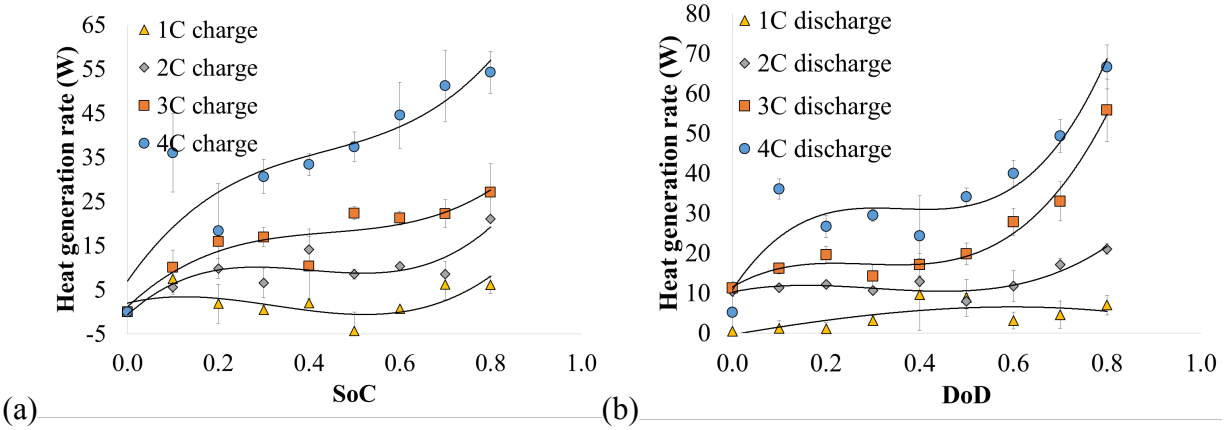

Figure 2.4: Heat generation rates (a) as a function of SoC during charging and (b) as a function of DoD during discharging at various current rates by temperature increase approach.

Both irreversible and reversible heat generation rates increase with the increase of current rate. Fig.2.4 is used to study the trend of heat generation rate with respect to SoC/DoD. The fitted equation of heat generation rate at various current rates are:

$$\dot{Q}(1C) = -9.05DoD^3 - 8.62DoD^2 + 20.02DoD - 0.41 \text{ [W] discharge} \quad (1.3.a)$$

$$\dot{Q}(1C) = 128.43SoC^3 - 124.63SoC^2 + 25.14SoC + 1.96 \text{ [W] charge} \quad (1.3.b)$$

$$\dot{Q}(2C) = 116.28DoD^3 - 105.71DoD^2 + 24.46DoD + 10.25 \text{ [W] discharge} \quad (1.3.c)$$

$$\dot{Q}(2C) = 210.14SoC^3 - 253.28SoC^2 + 93.01SoC - 0.67 \text{ [W] charge} \quad (1.3.d)$$

$$\dot{Q}(3C) = 293.87DoD^3 - 253.11DoD^2 + 68.50DoD + 11.51 \text{ [W] discharge} \quad (1.3.e)$$

$$\dot{Q}(3C) = 148.60SoC^3 - 198.34SoC^2 + 96.67SoC + 1.13 \text{ [W] charge} \quad (1.3.f)$$

$$\dot{Q}(4C) = 439.05DoD^3 - 439.80DoD^2 + 141.74DoD + 20.37 \text{ [W] discharge} \quad (1.3.g)$$

$\dot{Q}(4C) = 183.64SoC^3 - 255.79SoC^2 + 150.44SoC + 6.48$ [W] charge (1.3.h)

It can be seen that the heat generation rate increases with the increase of current rate [13] during both charge and discharge. The increase of current rate increases both irreversible and reversible heat. The increase in irreversible heat with the current rate is higher than that of the reversible heat. All the trends of heat generation are non-linear and S-shaped as obtained in previous studies on lithium-ion batteries [7].

The rate of heat generation during charging is always lower than rate of heat generation during the discharging process by up to 47.8%. The difference may be due to the reversible heat, which is endothermic during charging and exothermic during discharging [7]. Fig. 2.5 shows averaged heat generation rate growth in terms of current rate. The figure depicts that the heat generation increases with increasing current rate for both charging and discharging.

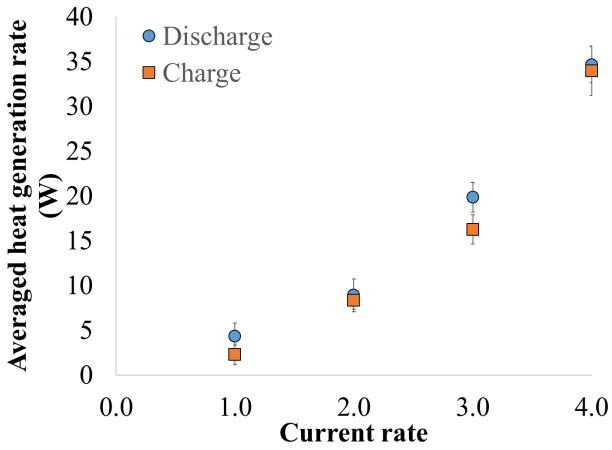

Figure 2.5: Comparison of averaged heat generation rate at various current rates for charging and discharging.

The fitted equation for the increase in average heat generation with current rate is given in eq (1.4):

$\dot{Q}_{average} = 1.87C^2 + 1.10C$ [W] for discharge (1.4.a)

$\dot{Q}_{average} = 2.27C^2 - 0.78C$ [W] for charge (1.4.b)

Where $\dot{Q}_{average}$ is the average heat generation and C is the current rate.

2.3.3.2 Comparison of heat generation characteristics using different methods

According to Bernadi model [12], the heat generation rate in the battery is determined by irreversible and reversible heats:

$$\dot{Q} = I \cdot (V - \mathrm{OCV}) - I \cdot T \cdot \frac{\partial \mathrm{OCV}}{\partial T} \tag{1.5}$$

Where I is the current, V is the operating voltage and OCV is the measured open circuit voltage. The irreversible heat I·(V-OCV) is generated by the ohmic loss, charge transfer resistance and mass transfer limitation, and the reversible heat (-I·T·∂OCV/∂T) is generated from the entropy change [9,18,19].

Besides the temperature increase method, this study also obtained heat generation characteristic using eq (1.5) for both charging and discharging at various current rates. The value of OCV was obtained as from the experiment described in section 2.1. Using the OCV values obtained using the experiment at each SoC and temperature, a look up table was created with recorded OCV values at each SoC and temperature. Hence, based on the known SoC and the temperature of the battery surface, OCV has been interpolated. As cited in literature, at higher current rates, the change in the magnitude of reversible heat is relatively small in comparison to the irreversible heat [12,14]. The reversible heat for both charging and discharging were equal in magnitudes and opposite in signs, which led to zero reversible heat generation in the cell over a cycle. Hence, only irreversible heat is considered in our study of the charge/discharge cycle at each current rate.

The heat generation is also evaluated using the over-potential between the charging and discharging voltages during a charging and discharging cycle at each SoC. This method provides an additional estimation of the heat generation during charge-discharge cycles. Fig. 2.6 shows the heat generation rate over a whole charge-discharge cycle at 1C, 2C, 3C and 4C current rates. The total heat generated by the battery using the above-mentioned methods at various discharge rates is summarized in Table 2.1.

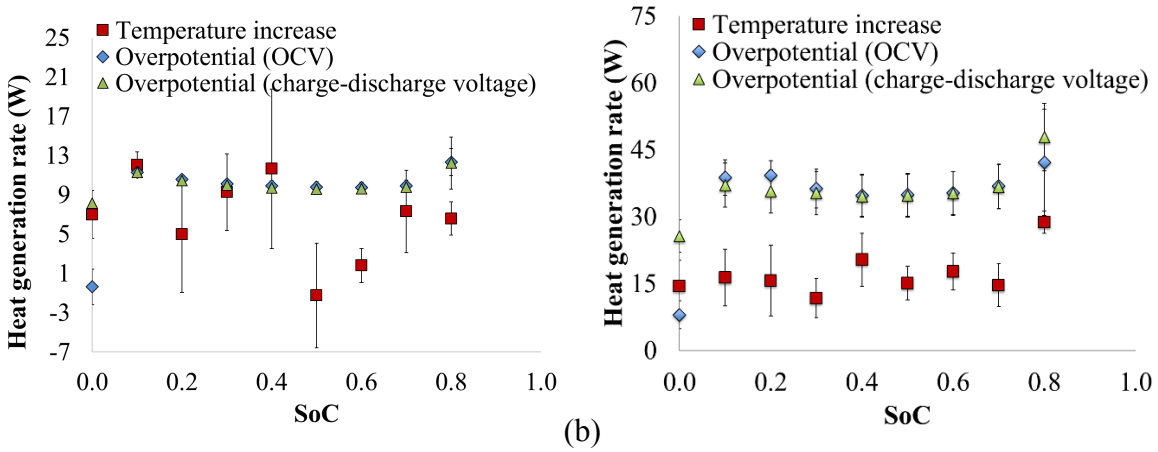

(a) (b)

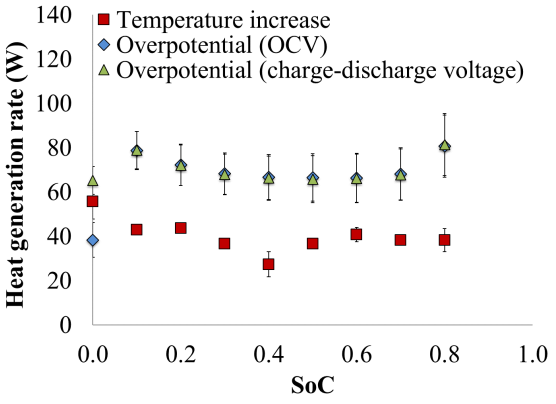

(c)

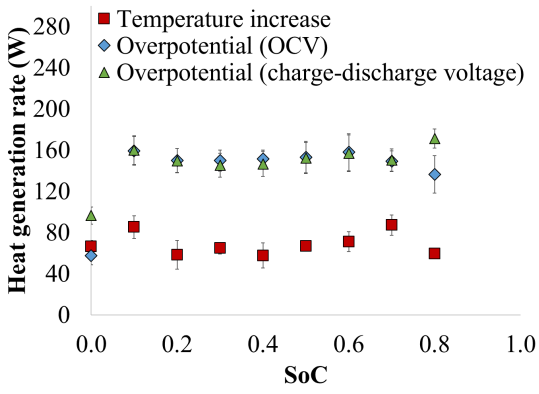

(d)

Figure 2.6: Comparison of heat generation characteristics of the battery for a charging and discharging cycle as a function of SoC at (a) 1C (b) 2C (c) 3C and (d) 4C current rates.

Table 2.1: Summary of the total heat generation using various methods at the end of cycle.

Rates	Overpotential using OCV (kJ)	Overpotential using charge-discharge voltage (kJ)	Temperature increase (kJ)
1C	30.34 ± 1.37	29.81 ± 0.75	17.58 ± 0.97
2C	54.29 ± 3.60	53.32 ± 6.66	30.66± 7.23
3C	68.71 ± 2.48	68.73 ± 10.58	42.13 ± 10.62
4C	110.66 ± 6.07	110.04 ± 8.76	52.06 ± 8.71

Results listed in Table 2.1 and Fig. 2.6 indicate that the heat generation rates obtained from the over-potential using OCV and overpotential using charge-discharge voltage are very similar. The total heat generation rates calculated by these methods have less than 3% difference at every SoC of the cycle. Both account for the total irreversible heat generation inside the battery cell using various voltage information.

At high current rates, the high heat generation rate leads to a significant temperature gradient within the battery [9] and on the surface of large batteries. The temperature gradient, as well as the time delay of temperature increase, results in significant experimental errors to estimate the amount of heat generation based on the heat absorption rate using the temperature increase of the battery surface and the cooling material. Hence, the temperature increase method underestimates the heat generation rate since it cannot completely consider the temperature gradient within the battery. In our following discussion, we can see that the temperature difference on a battery surface could be very significant, especially at high current rates. The amount of heat generation

results estimated by the temperature increase method underestimates the heat generation by 40.4, 43.1, 36.4 and 51.6% at 1, 2, 3 and 4C current rate respectively.

2.4 Maximum temperature difference on the battery surface

An important impact of the heat generation of a battery is the temperature difference on its surface, which affects the lifetime and efficiency of the battery [16]. Hence, the maximum temperature differences on the battery surface using air, aluminum foam, PCM, water and water with aluminum foam as cooling materials were studied at 1, 2 and 3C current rates and are shown in Fig. 2.7. The properties of each cooling materials are listed in Table 2.2. The maximum temperature on the battery surface was obtained near electrodes i.e. at thermocouple location 4 and 5 on Fig. 2.2 and the minimum temperature was obtained at the bottom of the battery (thermocouple location 1).

Table 2.2: Summary of the properties of various cooling materials.

Material	Mass (kg)	Specific heat capacity (J/kg/K)	Total heat capacity (J/K)	Thermal conductivity (W/m/K)
Air	2.45×10^{-5}	1000	0.024	0.026
Foam + air	8.08×10^{-2}	895	72.31	6.85 [20,21]
PCM	0.4911	2160	1060.98	0.36
Water	0.637	4200	2679.26	0.60
Water+foam	0.57(water) 8.08×10^{-2} (foam)	4200 (water) 895 (foam)	2466.31	7.66 [21]

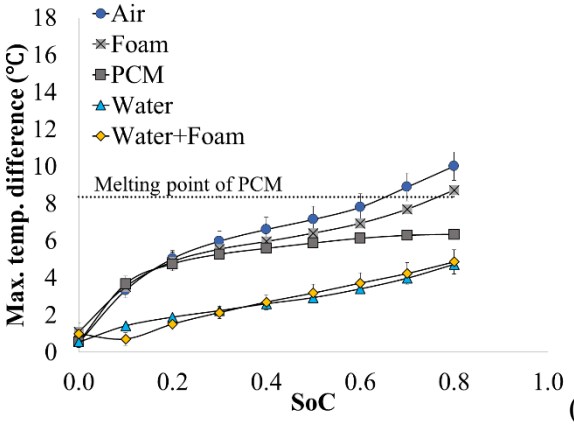

(a)

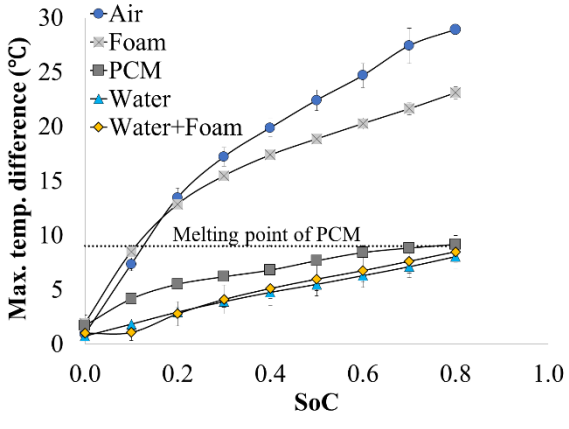

(b)

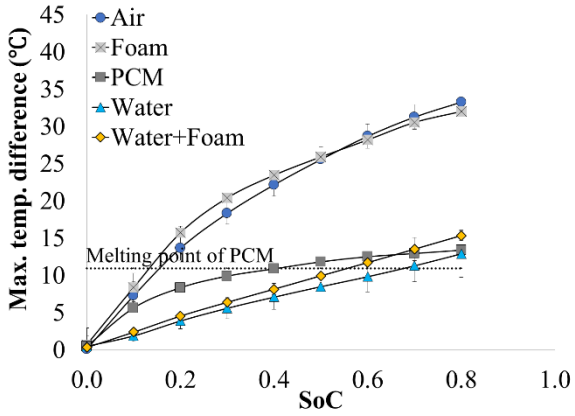

(c)

Figure 2.7: Comparison of surface temperature difference on the battery as a function of SoC using different cooling materials at (a) 1C (b) 2C and (c) 3C discharge.

All three results in Fig. 2.7 show that water, water with aluminum foam and PCM exhibit the lowest temperature differences throughout the battery surface for all discharge rates. Air results in the highest temperature difference on the battery surface followed by the foam at each current rate. The temperature differences between air and aluminum foam differ by around 2 to 3°C. The maximum temperature difference as seen in Fig. 2.7 increases significantly at higher current rates. In Fig. 2.7(a), maximum temperature difference of 7.7^{o}C is obtained using air as the cooling material. While the maximum temperature increase of 28.1^{o}C and 33.3°C was observed at 2C and 3C current rate respectively using air in Fig. 2.7(b)(c).

The battery cooled by PCM has slightly higher maximum temperature difference than the battery cooled by water and water with foam because of its lower total heat capacity as well as the lower thermal conductivity compared to the other two as shown in Table 2.2. At 2C and 3C current rates, the PCM melted and the melting of PCM could store a large amount of heat through the latent heat of PCM. The maximum temperature differences on the battery surface using PCM was 6.3, 9.1 and 13.1^{o}C respectively at 1, 2 and 3C current rate. The maximum temperature differences using water are 4.7, 8.4 and 12.9^{o}C at 1, 2 and 3C current rate respectively. Water with foam also resulted in similar maximum temperature differences with that using water i.e. 4.8, 8.4 and 15.3^{o}C at 1, 2 and 3C current rate respectively.

2.5 Average temperature increase of the battery surface

In order to study the effectiveness of various passive cooling materials, the increase of average surface temperature of the battery with SoC is also measured at different current rates. Average surface temperature of the battery refers to the average value of the readings from the 5

thermocouples attached on the battery surface. Fig. 2.8 shows the trend of temperature increase with different cooling materials at each current rate.

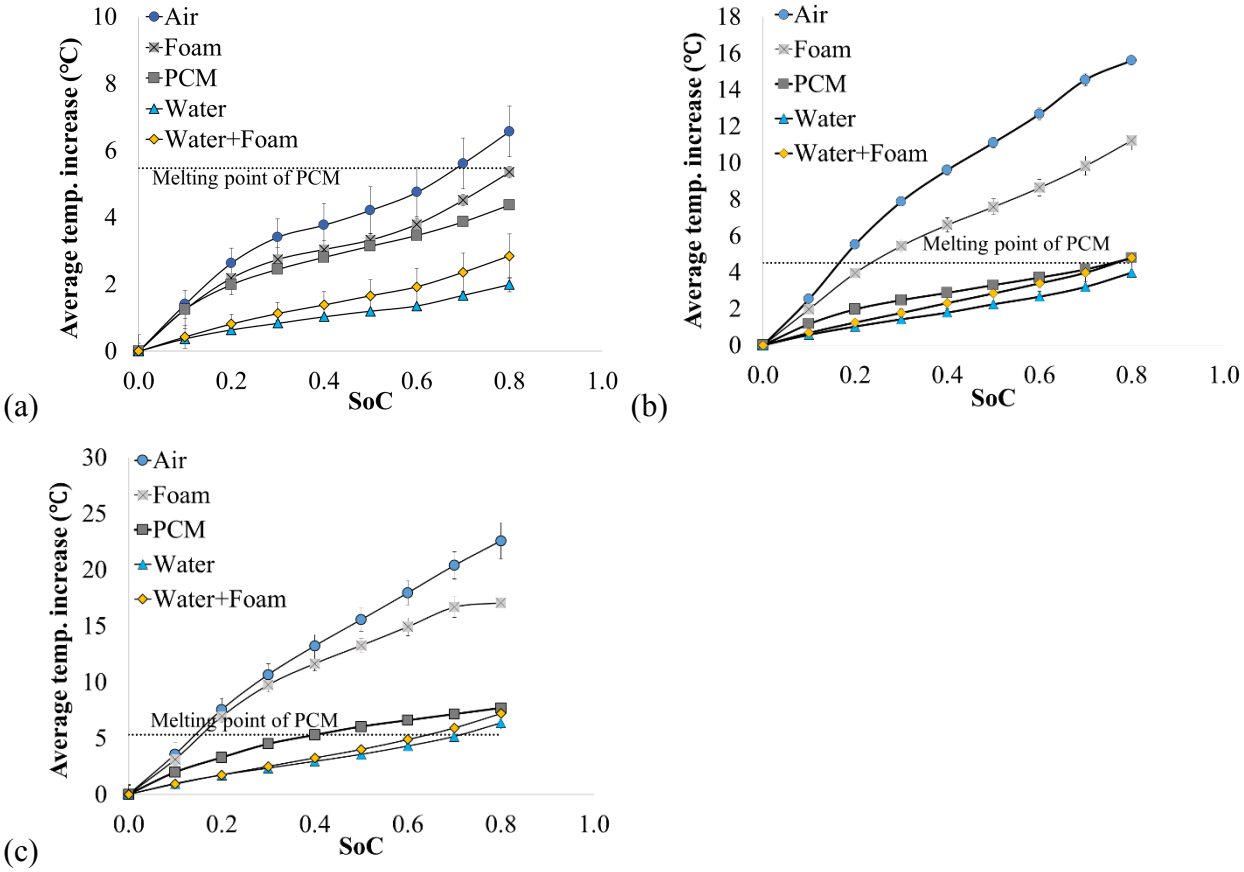

Figure 2.8: Comparison of average temperature increase on the battery surface as a function of SoC using various cooling materials at (a) 1C (b) 2C and (c) 3C current rates.

It can be seen from Fig. 2.8 (a) that, the increase in average temperature of battery surface increases with the increase in the current rate [22]. The average temperature increase with air is the highest i.e. approximately 6.5°C at 1C, 15.5°C at 2C and 22.5°C at 3C current rate due to the very low thermal conductivity as well as the low heat capacity of the air. Aluminum foam maintains an average temperature lower by approximately 4°C since it has relatively higher thermal conductivity and heat capacity.

Initially, PCM results in a higher increase in average temperature compared to water or water with foam due to its slightly lower thermal conductivity as seen in Fig. 2.8 (c). Later, it can be seen that the average temperature of the battery using PCM slows down as soon as the phase change temperature is reached. The phase change of PCM helps to store heat as latent heat and maintain lower average temperature on the battery surface. This behavior is similar to the result

obtained in references [22-25]. PCM shows promising application especially at high discharge rates and/or in battery packs composed of multiple single cells because of its phase change property [22,24-26].

Fig. 2.8 also shows that the average surface temperature of the battery using only water is slightly lower than the average temperature using water with aluminum foam. Use of aluminum foam (0.9 porosity) with water results in about 10% volume decrease of water compared to the setup with only water. As it can be seen in Table 2.2, the heat capacity of water is higher compared to aluminum. The total heat capacity using the water with foam as cooling material is 7.9% lower than the heat capacity of pure water. As a result, the average temperature of the battery when cooled using water with foam is slightly higher than using only water. The loss in quantity of water used affects the overall heat dissipation. With the same volume, water, water with aluminum foam and PCM exhibit the desired property to maintain lower average temperature and lower temperature gradient on the battery surface compared to air and aluminum foam.

2.6 Conclusion

Fundamental thermal properties of the lithium-ion battery along with the heat generation characteristic of the battery were studied. The heat generation rate during discharging process was higher than the heat generation rate during charging process, which can be attributed to the slightly endothermic behavior observed during the charging process. The heat generation rate as well as the total heat generated by the battery increased with the increase in the current rate. The effectiveness of several cooling materials used in passive thermal management system to maintain lower battery surface temperature and low surface temperature gradient has been studied. Results showed that cooling by natural convection of air only might result in high temperature increase and high temperature gradient on the battery surface (up to 60^{o}C at 3C current rate). Aluminum foam showed better cooling effects than air while water, PCM and water with aluminum foam are more desirable. Using PCM, water or water with aluminum foam as the cooling material, the average temperature increases at the surface are less than 8^{o}C and the maximum temperature differences at the surface are less than 16^{o}C even at the current rate of 3C. For such low average surface temperature increases on the battery surface using PCM, water and water with aluminum foam for cooling, the inside temperature of the battery will also stay within the safe limit despite the 42.8% underestimation of heat generation that we obtained using the

temperature increase method considering only the battery surface temperature for heat generation estimation.

Nomenclature:

Acronyms

SoC	State of Charge
DoD	Depth of Discharge
OCV	Open Circuit Voltage
PCM	Phase Change Material

Variables

$\partial OCV/\partial T$	Entropy coefficient
T	Temperature
Q	Heat generated
$\dot{Q}$	Heat generation rate
m	Mass
c_p	Specific heat capacity
I	Current
R	Resistance
V	Voltage

References:

[1] B. Scrosati, J. Hassoun, Y. Sun, Lithium-ion batteries. A look into the future, Energy and Environmental Science. 4 (2011) 3287-3295.

[2] L. Yuan, Z. Wang, X. Hu, J. Chen, Y. Huang, J. B. Goodenough, Development and challenges of LiFePO4 cathode material for lithium-ion batteries, Energy & Environmental Science. 4(2011) 269-284.

[3] Q. Wang, P. Ping, X. Zhao, G. Chu, J. Sun, C. Chen, Thermal runaway caused fire and explosion of lithium ion battery, Journal of Power Sources. 208 (2012) 210-224.

[4] Q. Huang, Mss. Yan, Z. Jiang, Thermal study on single electrodes in lithium-ion battery, Journal of Power Sources. 156 (2006) 542-546.

[5] J. Groot, M. Swierczynski, A.I. Stan, S.K. Kaer, On the complex ageing characteristics of high-power LiFePO4/graphite battery cells cycles with high charge and discharge currents, Journal of Power Sources. 286 (2015) 475-487.

[6] L. Lu, X. Han, J. Li, J. Hua, M. Ouyang, A review on the key issues for lithium-ion battery management in electric vehicles, Journal of Power Sources. 226 (2013) 272-288.

[7] C. Lin, S. Xu, Z. Li, B. Li, G. Change J. Liu, Thermal analysis of large-capacity $LiFePO_4$ power batteries for electric vehicles, Journal of Power Sources. 294 (2015) 633-642.

[8] K. Takano, Y. Saito, K. Kanari, K. Nozaki, K. Kato, A. Negishi, T. Kato, Entropy change in lithium ion cells on charge and discharge, Journal of Applied Electrochemistry. 32 (2002) 251-258.

[9] T.M. Bandhauer, S. Garimella, T.F. Fuller, Temperature-dependent electrochemical heat generation in a commercial lithium-ion battery, Journal of Power Sources. 247 (2014) 618-628.

[10] C. Forgez, D.V. Do, G. Friedrich, M. Morcette, C. Delacourt, Thermal modeling of a cylindrical $LiFePO_4$/graphite lithium-ion battery, Journal of Power Sources. 195 (2010) 2961-2968.

[11] S.J. Drake, D.A. Wetz, J.K. Ostanek, S.P. Miller, J.M. Heinzel, A. Jain, Measurement of anisotropic thermophysical properties of cylindrical Li-ion cells, Journal of Power Sources. 252 (2014) 298-304.

[12] D. Bernardi, E. Pawlikowski, J.Newman, A general energy balance for battery systems, Journal of the Electrochemical Society. 132 (1985) 5-12.

[13] M. Yildiz, H. Karakoc, I. Dincer, Modeling and validation of temperature changes in a pouch lithium-ion battery at various discharge rates, International Communications in Heat and Mass transfer. 75 (2016) 311-314.

[14] K. Chen, G. Unsworth, X. Li, Measurement of heat generation in prismatic Li-ion batteries, Journal of Power Sources. 261 (2014) 28-37.

[15] K. Chen, X. Li, Accurate determination of battery discharge characteristics-A comparison between two battery temperature control methods, Journal of Power Sources, 247 (2014) 961-966.

[16] M. Alipanahrostami, X. Li, Numerical Studies of Lithium-ion Battery Thermal Management System Using Phase Change Materials and Metal Foams, International Journal of Heat and Mass Transfer. 102 (2016) 1159-1168.

[17] W. Libeer, F. Ramos, C. Newton, M. Alipanahrostami, C. Depcik, X. Li, Two-phase heat and mass transfer of phase change materials in thermal management systems, International Journal of Heat and Mass Transfer. 100 (2016) 215-223.

[18] S. Panchal, I. Dincer, M. Agelin-Chaab, R. Fraser, M. Fowler, Experimental and theoretical investigations of heat generation rates for a water-cooled LiFePO4 battery, International Journal of Heat and MassTransfer, 101 (2016) 1093-1102.

[19] S. Panchal, I. Dincer, M. Agelin-Chaab, R. Fraser, M. Fowler, Thermal modeling and validation of temperature distributions in a prismatic lithium-ion battery at different discharge rates and varying boundary conditions, Applied Thermal Engineering. 96 (2016) 190-199.

[20] F. Wang, X. Li, The stagnant thermal conductivity of porous media predicted by the random walk theory, International Journal of Heat and Mass Transfer. 107 (2017) 520-523.

[21] R. Singh, H.S. Kasana, Computational aspects of thermal conductivity of highly porous metal foams, Applied Thermal Engineering. 24 (2004) 1841-1849.

[22] R. Kizilel, A. Lateef, R. Sabbah, M.M. Farid, J.R. Selman, S. Al-Hallaj, Passive control of temperature excursion and uniformity in high-energy Li-ion battery packs at high current and ambient temperature, Journal of Power Sources. 183 (2008) 370-375.

[23] W.Q. Li, Z.G. Qu, Y.L. He, Y.B. Tao, Experimental study of a passive thermal management system for high-powered lithium ion batteries using porous metal foam saturated with phase change materials, Journal of Power Sources. 255 (2015) 403-410.

[24] J. Yan, K. Li, H. Chen, Q. Wang, J. Sun, Experimental study on the application of phase change material in the dynamic cycling of battery pack system, Energy Conversion and Management. 128 (2016) 12-19.

[25] R. Sabbah, R. Kizilel, J.R. Selman, S. Al-Hallaj, Active (air-cooled) vs. passive (phase change material) thermal management of high power lithium-ion packs:Limitation of temperature rise and uniformity of temperature distribution, Journal of Power Sources. 182 (2008) 630-638.

[26] K. Onda, T. Oshima, M. Nakayama, K. Fukuda, T. Araki, Thermal behavior of small lithium-ion battery during rapid charge and discharge cycles, Journal of Power Sources. 158 (2006) 535-542.

3. Modeling

3.1 Introduction

Battery modeling is crucial to design an optimum cell with desired configurations. The heat generation in a battery is a complex process that couples with electrochemical reactions [1]. Experiments help to understand the physical chemistry of materials used in the battery whereas the electrochemical model help in understanding the internal transport phenomena that cannot be assessed through the experiments. All these information aid in the optimization of battery design [2]. The electrochemical model can also be used to estimate essential battery parameters like current, voltage and temperature in order to regulate them through proper battery management systems [3]. These estimations help researchers to better understand the design limitations and internal electrochemical behavior of batteries [4].

Fundamental battery models as used in the current work is derived from the porous electrode theory that describe species and charge transport in the solid matrix and the liquid electrolyte phase across a simplified 1D structure. It can be then solved numerically in a computational fluid dynamics framework by discretizing the coupled partial differential equations to a set of ordinary differential equations to be solved iteratively [5]. In order to build a robust battery model that can accurately predict the electrochemical and the thermal properties of a battery, the proper estimation of the model parameters is necessary [6].

The thermal management of a battery is one of the major concerns affecting the performance and lifetime of a lithium ion battery. Thus, researchers are working on developing various types of electrical and electrochemical models that are coupled with the thermal model in order to better understand the electrochemistry and its effect on the thermal behavior of a battery. Several models such as pseudo-2D models, single particle models are constantly studied and simplified to predict a battery's electrochemical and thermal characteristics. The thermal model combined with single particle models and assuming constant local reaction current are more efficient when the current rate is below 1C [7]. With suitable assumptions and parameter estimation, the combined model can also be used for predicting the battery behavior above 1C current rate. More complex model such as pseudo-2D porous model and polynomial approximation porous model are considered more efficient in characterizing battery behavior above 1C current rate [7].

The temperature of a battery in a model is obtained based on the heat generation and dissipation rates. The heat generation, active polarization, entropy change, and resistance in a battery is mainly contributed by electrochemical reactions [6,8]. The overpotential and resistance due to the electrochemical reactions contribute towards the irreversible heat generation and the entropy change inside the battery contribute towards the reversible heat generation. Ye et al. [6] developed a quasi 2D mathematical model for an 11.5Ah $LiMn_2O_4$ prismatic battery by coupling electronic conduction, mass transfer, energy balance and electrochemical mechanism. This study found that the influence of reversible heat on battery discharge was negligible for high current rates.

The heat generation across a large battery is not uniform throughout. Without proper cooling systems, hot spots can build up within a battery and result in possible thermal runaway. Huang et al. [9] studied the thermal behavior of each electrode based on the reversible heat generation during the discharge process of a fully charged $LiCoO_2$ battery. It was seen that the cell discharge process is an exothermic reaction with entropy change of -29.78 J K^{-1} mol^{-1} and reversible heat generation of 8.874 kJ mol^{-1}. The heat produced at the positive electrode was found to be higher than that of the negative electrode. This phenomenon should be taken into consideration to design thermal system when batteries operate at high current rates.

Typical thermal models require several information related to heat transfer based on geometry and thermal properties of a battery such as the convection coefficient, Nusselt's number etc in order to simulate proper heat dissipation from the surface at different conditions. Similarly, solving for the solid and electrolyte concentrations, solid and electrolyte potentials, and the overpotential of a battery requires proper estimations or experimental measurements of several electrochemical properties such as the diffusion coefficient, ionic conductivity etc. Thus, a battery model without simplification requires long computational time because of the complexity involved in solving the discretized equations, and the large number of parameters involved. This also limits the use of an electrochemical model in simulating the behaviors of battery packs [10]. Thus, reliable and fast models are desired for the real time applications [5,11].

The model presented in this work is a simplified 1D electrochemical-thermal coupled model along the thickness of a $LiFePO_4$ battery that is capable of providing the required electrochemical and thermal details with good accuracy. The model couples the battery

electrochemical model with the thermal model, and the computational domain includes not only the battery but also the passive cooling material around the battery. The lithium ion concentration and its gradient in the electrolyte phase is one of the important factors governing the heat generations characteristics of a battery especially at high current rates [7,8]. Therefore, the electrolyte concentration across the battery components is solved and coupled with the Butler-Volmer equation to predict the overpotential and the current density distribution inside the battery. The overpotential and the current density information are then used to predict the temperature within the battery and the cooling material as well as the heat generation characteristics of the battery.

The heat conduction throughout the entire modeling domain, which includes the battery as well as the passive cooling material, does not require additional estimations or assumptions of the heat dissipation at the interface of the battery and the cooling material. Thus, the heat generation characteristic of the battery only requires the thermal physical properties such as thermal conductivity, density, and specific heat capacity of each component. The model can also be used to study the temperature change of the cooling material and the battery's surface temperature in order to study the effectiveness of a desired cooling material at any current rates. Unlike other models reported in the literature, the electrochemical-thermal model presented in this work requires solving of fewer governing equations that helps to reduce the complexity and computational cost of the model without compromising the accuracy. This characteristic of the model is desired for the real-time application of the battery model to battery management system.

3.2 Model development

This electrochemical-thermal coupled model first solves the electrochemical equations in order to obtain the overpotential, which is later incorporated into a thermal model to solve for the temperature. A 1-D domain along the thickness of lithium ion battery is developed. A schematic diagram showing various components of a lithium-ion battery configuration considered for the modeling purpose is shown in Fig. 3.1. Five different components of a battery are included in the model: two current collectors (CC), two electrodes, and a separator. The anode current collector is made of copper whereas the cathode current collector is made of aluminum. A layer of cooling material is considered on each side of the battery for the purpose of passive cooling. The

thickness of each layer is listed in Table 3.1. The total length of the setup is L and each consecutive x represents the length from zero to that point

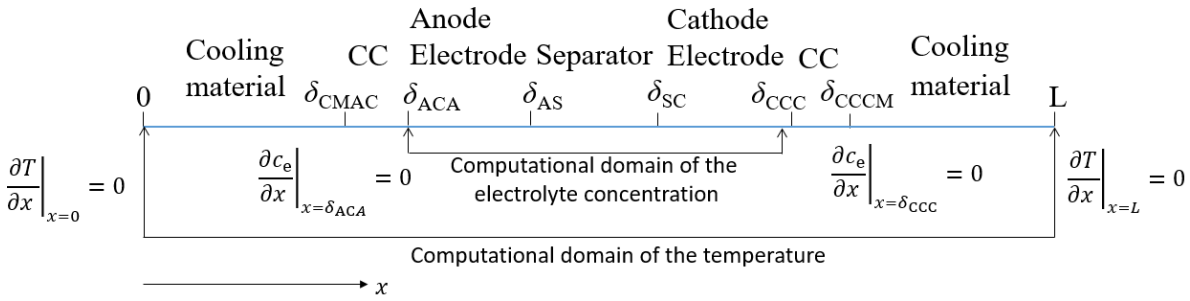

Figure 3.1: The computational domain of a lithium-ion cell (not to scale).

In Fig. 3.1, x_{CMAC}, x_{ACA}, x_{AS}, x_{SC}, x_{CCC}, x_{CCCM} are the locations of the cooling material-anode current collector interface, the anode current collector-anode electrode interface, the anode electrode-separator interface, the separator-cathode electrode interface, the cathode electrode-cathode current collector interface, and the cathode current collector-cooling material interface respectively. The performance of a battery is characterized by four different partial differential equations describing the time evolution of lithium concentration in the electrode and electrolyte phases under charge conservation. The energy balance equation is solved to calculate the temperature distribution at each layer. The heat generation (source term) in each layer required for the thermal model is estimated by calculating the over-potential using the Butler-Volmer equation at each electrode (i.e. cathode and anode) as well as the ohmic resistance. No heat generated in the separator since there is no reaction. All governing equations and boundary conditions are listed in the section below.

3.2.1 Electrochemical model

The electrodes are modeled using the porous electrode theory, where the solid and electrolyte phase are considered to exist superimposed to each other. The electrolyte phase is continuous along the entire battery whereas the electrically conducting phase (solid) exists only in the electrodes. The current density in anode and cathode electrodes can be expressed by eq. (3.1) and (3.2) respectively,

$$\frac{I}{A} = \int_{x_{ACA}}^{x_{AS}} j_a \cdot dx \tag{3.1}$$

$$-\frac{I}{A} = \int_{x_{SC}}^{x_{CCC}} j_c \cdot dx \tag{3.2}$$

Where I is the total current (A), A is the geometric area (m^2), j is the current density (A/m^2), and the subscripts 'a' and 'c' denotes anode and cathode respectively. The Butler-Volmer equation as listed in eq (3.3) couples the current, concentration, and overpotential distribution at the solid/electrolyte interface [4,8]. The current density distribution along the battery electrodes can be then obtained using eq (3.3) in each electrode.

$$j\,(x) = \frac{C_{\mathrm{e}}}{C_{\mathrm{e,ref}}} \cdot j_{\mathrm{o}} \cdot a_{\mathrm{s}} \left(\exp\left(\frac{\alpha_{\mathrm{a}} \cdot F \cdot \eta}{R \cdot T} \right) - \exp\left(\frac{-(1-\alpha_{\mathrm{c}}) \cdot F \cdot \eta}{R \cdot T} \right) \right) \tag{3.3}$$

Where $C_{\mathrm{e,ref}}$ is the reference electrolyte concentration (1500 mol/m^3), j_0 is the exchange current density (A/m^2) [10,13], a_s is the active surface area (m^{-1}), α is the charge transfer coefficient, η is the overpotential (V), F is the Faraday's constant (96,487 C/mol), R is the universal gas constant (8.314 J/kg/K), and T is the absolute temperature (K). The active surface area of each electrode is is determined by [12-17].

$$a_{\mathrm{s}} = 3\varepsilon_{\mathrm{s}} / R_{\mathrm{sp}} \tag{3.4}$$

Where ε_s is the solid phase porosity of the electrode, and R_{sp} is the radius of the solid particle in the electrode (m). Conservation equation of lithium ion in the electrolyte phase is

$$\frac{\partial(\varepsilon_{\mathrm{e}} c_{\mathrm{e}})}{\partial t} - \partial\left(D_{\mathrm{e}}^{\mathrm{eff}} \frac{\partial}{\partial x} c_{\mathrm{e}} \right) = \frac{1-t_+^0}{F}\, j \tag{3.5}$$

Where c_e is the electrolyte concentration (mol/m^3), $\mathcal{E}_e$ is the electrolyte phase volume fraction, D_e^{eff} is the effective lithium ion diffusion coefficient in the electrolyte phase (m^2/s), t_+^0 is the lithium ion transference number, and j is the current density (A/m^3). The initial electrolyte concentration, $C_{e,0}$ is assumed to be 1500 mol/m^3. The solution is constrained by no flux boundary conditions at the electrode-current collector interfaces:

$$\left.\frac{\partial c_{\mathrm{e}}}{\partial x}\right|_{x=x_{\mathrm{ACA}}} = \left.\frac{\partial c_{\mathrm{e}}}{\partial x}\right|_{x=x_{\mathrm{CCC}}} = 0 \tag{3.6}$$

The effective diffusion coefficient is calculated using Bruggman relation given by

$$D_{\mathrm{e}}^{\mathrm{eff}} = D_{\mathrm{e}} \varepsilon_{\mathrm{e}}^{1.5} \tag{3.7}$$

3.2.2 Thermal model

The energy equation is used to estimate the temperature distribution, which utilizes the overpotential and reaction rates obtained from the electrochemical model as a source term. The heat generated due to overpotential in the anode and cathode electrodes, $\dot{q}_{\mathrm{a}}$ and $\dot{q}_{\mathrm{c}}$ can be estimated by:

$$\dot{q}_{\mathrm{a}} = \int_{x_{\mathrm{ACA}}}^{x_{\mathrm{AS}}} j_{\mathrm{a}} \cdot \eta_{\mathrm{a}}\, dx \tag{3.8}$$

$$\dot{q}_{\mathrm{c}} = \int_{x_{\mathrm{SC}}}^{x_{\mathrm{CCC}}} j_{\mathrm{c}} \cdot \eta_{\mathrm{c}}\, dx \tag{3.9}$$

The internal resistance of the battery (R_{int}) also contributes to the heat generation in the battery as the ohmic loss. The heat generation rate due to the internal resistance in the battery is given by eq (3.11) [10].

$$\dot{q_{\Omega}} = I^2 R_{\mathrm{int}} \tag{3.11}$$

Where $\dot{q_{\Omega}}$ is the heat generation rate due to the internal resistance (W/m^3) of the battery. The total heat generation rate ($\dot{q}$) in both electrodes can be expressed as in eq (3.12).

$$\dot{q} = \dot{q}_{\mathrm{a}} + \dot{q}_{\mathrm{c}} + \dot{q}_{\Omega} \tag{3.12}$$

The temperature distribution in the cell along each component is estimated by solving the transient one-dimensional heat conduction equation as listed in eq (3.13).

$$\rho c_p \frac{\partial T}{\partial t} = k \frac{\partial^2 T}{\partial x^2} + \dot{q} \tag{3.13}$$

Where ρ is the density (kg m^{-3}), c_p the specific heat capacity (J kg^{-1} K^{-1}), T is the temperature (K), k is the thermal conductivity (W m^{-1} K^{-1}) of each component. The initial battery surface temperature is T_0. The boundary conditions on the left and right boundaries i.e at the end of the cooling materials are assumed to be insulated as our experimental setup design.

$$-k \frac{\partial T}{\partial x}\Big|_{x=0} = 0 \tag{3.14}$$

$$-k \frac{\partial T}{\partial x}\Big|_{x=L} = 0 \tag{3.15}$$

3.3 Solution approach

The model was solved using the finite volume method for each governing equation and boundary conditions using a self-developed Matlab code. The finite volume method is advantageous when rigorous conservation equations are very important in simulating a physical system. This is often the case in transient simulations of internal flows or thermally isolated systems. The finite volume method uses volume integral formulations with finite partitioning set of volumes to discretize the governing equations.

The solution method used to solve the model applying the finite volume method is discussed in detail in the Appendix. A few simulations were also run to validate the model using different node numbers to check for the grid independence. In addition to that, the model was also validated by comparing the results obtained at different time steps and tolerance values between two consecutive iterations. The details of the validation are also discussed in the Appendix.

Each battery component as well as the cooling material are of different lengths. Hence, each component was discretized using different number of nodes to get a constant node length throughout the entire modeling domain. The total number of nodes used across the entire modeling domain was 2,691 with the node size of 8.26×10^{-6} m. The tolerance of 10^{-7} and time steps of 7.2 s, 3.6 s and 2.4 s at 1C, 2C and 3C current rate respectively were used in the code. Fig. 3.2 is a flowchart showing the steps used to solve the model.

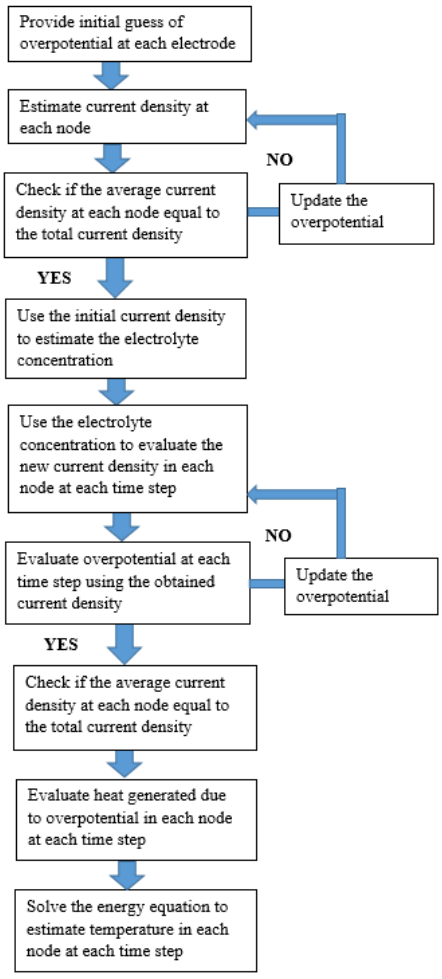

Figure 3.2: The flowchart of the steps to solve the model.

3.4 Parameters

All the parameters used in equations discussed above are listed in Table 3.1 below.

Table 3.1: Electrochemical and thermal parameters of the battery components

Property	Anode	Cathode	Separator	Anode CC	Cathode CC
Thickness (m)	3.28×10^{-3}	2.11×10^{-3}	0.93×10^{-3}	4.63×10^{-4}	4.63×10^{-4}

α	0.5	0.5	-	-	-
j_o (Am^{-2})	0.5	0.05	-	-	-
R_s (m)	0.85×10^{-5} [2]	1.25×10^{-5} [2]	-	-	-
A (m^2)	0.036	0.036	-	-	-
k ($W\ m^{-1}\ K^{-1}$)	1.04 [18]	1.48 [18]	1[18]	400 [19]	160 [189]
ρ ($kg\ m^{-3}$)	2660 [19]	1500 [19]	492 [19]	8900 [19]	2700 [19]
c_p ($J\ kg^{-1}\ K^{-1}$)	1437 [19]	1260 [19]	700 [19]	385 [19]	903 [19]
ε_e	0.3 [19]	0.28 [19]	0.4 [19]	-	-
ε_s	0.435 [19]	0.56 [19]	-	-	-
D_e (m^2/s)	9.2×10^{-7}	9.2×10^{-7}	9.2×10^{-7}	-	-
R ($J\ mol^{-1}K^{-1}$)	8.314	-	8.314	-	-
F (C/mol)	96487	-	96487	-	-
t_+	0.363	0.363	0.363	-	-
R_c (Ohms)	0.0006	0.0006	-	-	-

The properties of the cooling material considered for the model is listed in Table 3.2.

Table 3.2: Properties of various cooling materials.

Property	Air	Water
k ($W\ m^{-1}\ K^{-1}$)	0.026	0.607
ρ ($kg\ m^{-3}$)	1.185	997.1
c_p ($J\ kg^{-1}\ K^{-1}$)	1005	4180

3.5 Results and discussion

Fig. 3.3 shows the electrolyte concentration inside the battery at various current rates. In the plots below: A indicates the anode region, S indicates the separator region, C indicates the cathode region, and CM indicates the cooling material region. From eq. 3.3 it can be seen that the gradient of the electrolyte concentration increases proportionally with the increase of the current rate. The lithium ion concentration in the anode is always higher than the cathode (Fig. 3.3) because the lithium ions are generated in the negative electrode and diffuse to the liquid phase. The lithium ions then intercalate to the positive electrode and decrease the liquid phase lithium concentration in the cathode. Based on the concentration gradient at each current rate, the

current density distribution at each electrode is evaluated using eq. (3.3). The current density distribution along the length of anode and cathode are shown in Fig. 3.4 (a) and (b), respectively.

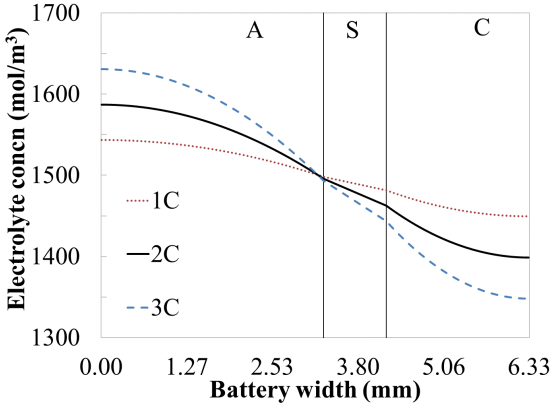

Figure 3.3: The electrolyte concentration along the battery components using various current rates at 0.8 DoD.

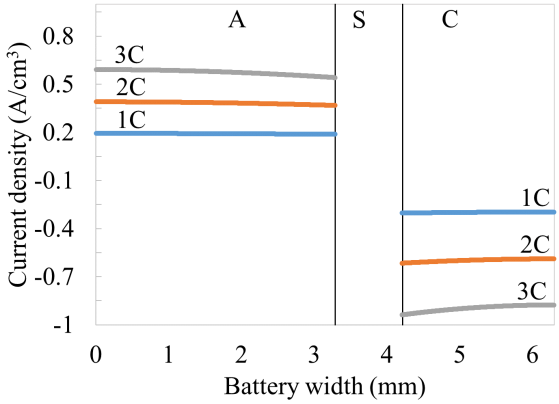

Figure 3.4: The current density distributions at the anode electrode (left) and the cathode electrode (right) at different current rates.

During the discharge process, anode releases electrons through the oxidation process, which are accepted by the cathode to complete the circuit for the electron flow. Thus, as seen in Fig. 3.4, the current density has positive value in the anode and negative value in the cathode. Also, the current density across the anode and cathode increases with the increase in the applied current and vice versa since they are directly related to the applied current as shown in eq. (3.1) and (3.2). Based on the same equations, the absolute value of total current density in both anode and cathode are always equal to the total applied current density of the battery. The distribution

of the current density across the electrodes is directly related to the electrolyte concentration. Therefore the current density has a more uniform distribution at 1C current rate because of the smaller concentration gradient at 1C current rate (Fig. 3.3). With the increase in the current rate, the current density has a higher gradient due to the higher concentration gradient of lithium ion obtained at higher current rates.

Using the current density distribution, the overpotential value at each electrode was estimated by solving eq (3.3) iteratively. The estimated values of overpotential at the anode and the cathode electrodes are shown in Fig. 3.5. Since the overpotential is directly proportional to the current rate as shown in eq. (3.3) by the Butler-Volmer relation, the overpotential in the anode and cathode have a positive and a negative sign respectively. The absolute value of the overpotential in each electrode also increases with the increase of the current density.

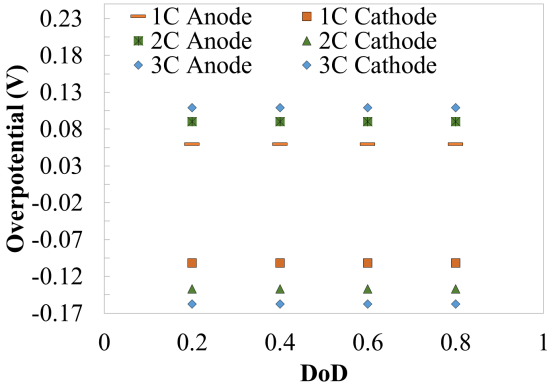

Figure 3.5: The variations of overpotential with the DoD at the (a) anode and (b) cathode at different current rates.

The heat generation rate caused by the overpotential is considered along the battery electrodes to determine the temperature. Similarly, the heat generation rate due to the internal resistance of the battery is considered on the entire electrode regions. The overpotential account for the activation loss and concentration loss while the internal resistance accounts for the ohmic loss in the battery. The resistance value of 0.6 mΩ was used for thsis simulation, which is the internal resistance of our battery measured in the lab. Fig. 3.6 shows the contribution of the internal resistance and the overpotential in the total heat generated by the battery.

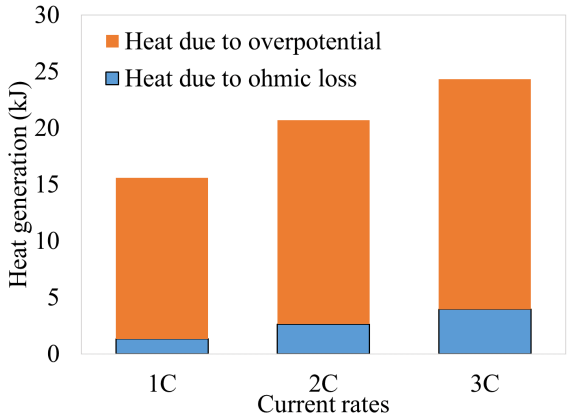

Figure 3.6: Comparison of the percentage contribution to the heat generation by the overpotential and ohmic loss.

As seen in Fig. 3.6, the ohmic loss contributes an average of 12.4% of the total heat generation and the rest is contributed by the activation and concentration overpotential. The total heat contribution by each loss increases with the increase in the applied current rate. Hence, ohmic loss does have a significant contribution in the total heat generated by the battery and cannot be neglected. Thus, proper measurement and understanding of the internal resistance of a battery is crucial. Both the heat generation rate due to the overpotential and the internal resistance comprise the irreversible heat generated inside the battery. The reversible heat generation rate was ignored in the simulation process also because they are negligible at high current rates as observed and discussed in the experimental chapter. The heat generation rate obtained at each electrode is shown in Fig. 3.7. As we can see in Fig. 3.7, the heat generation rate in electrode increases proportionally with the increase in the current density. Higher heat generation rates are obtained in the cathode region due to the higher current density and overpotential in the cathode region. Considering the heat generation rate as the source term ($\dot{q}$) in our energy equation listed in eq. (3.13), the temperature distribution at each node along the entire modeling domain was obtained at various current rates and DoDs.

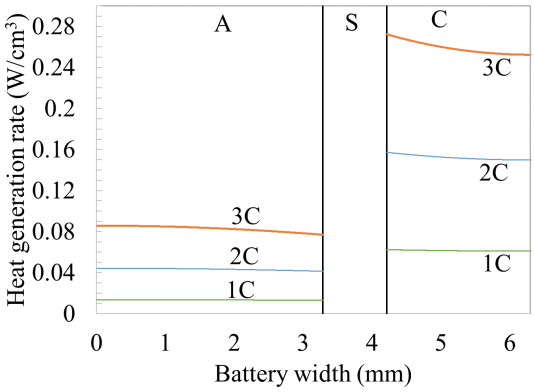

Figure 3.7: The heat generation rate at the anode electrode (left) and the cathode electrode (right) at different current rates.

Fig. 3.8 shows a comparative plot of the temperature distribution along our modeling domain at different current rates. As we can see from eq. (3.5), (3.6) and (3.7), that the heat generation rate due to both the overpotential and the internal resistance is directly proportional to the applied current to the battery. In Fig. 3.8 (a) and (b), we observe a higher increase in the temperature across the cooling material as well as within the battery with the increase in the current rate irrespective of the cooling material used. In Fig. 3.8 (b), the temperature increase in the case with air as the cooling material is higher because of the lower density and specific heat capacity of the air as listed in Table 3.2. The lower density and specific capacity result in a lower heat absorption capability that in turn results in a faster increase in the temperature of the surrounding as well as the battery when using air as the cooling material

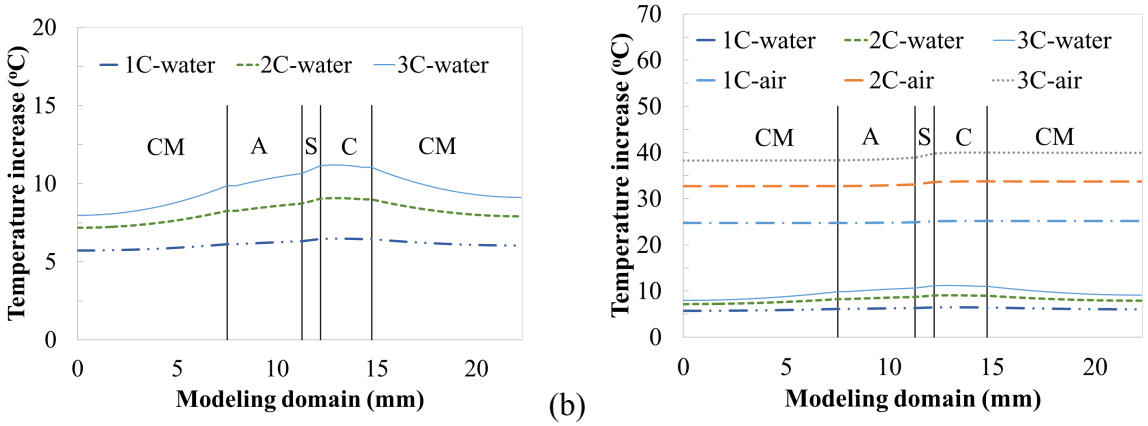

Figure 3.8: Comparison of the distribution of temperature increase (a) using water as the cooling material and (b) using air and water as the cooling material at 0.8 DoD.

Fig. 3.9 shows the comparison of the battery surface temperature at each current rate and various DoD using air and water as the cooling materials. The surface temperature of the battery is measured at the cathode current collector-cooling material interface (x_{CCCM}) in the modeling domain as shown in Fig. 3.1. The battery surface temperature using air as the cooling material is always higher than the battery surface temperature using water as the cooling material due to its lower heat absorbing capacity. The model always over predicts the temperature value at the battery surface than the experiment, which might be because of the losses present in the experimental setup. During the experimental measurements, using air as the cooling material, high temperature values and a large temperature gradient is observed on the battery surface. Such high value of surface temperature and temperature gradient results in higher heat losses during the experiment at high current rates. This might be the reason for the over prediction of the battery surface temperature using air as the cooling material. Tables 3.3, 3.4, and 3.5 lists the temperature on the battery surface at several DoD using air and water as the cooling material at 1C, 2C, and 3C current rate respectively.

Table 3.3: The battery surface temperature using air and water as the cooling material at 1C current rate

DoD at 1C	Experiment (Air)	Simulation (Air)	% Error	Experiment (Water)	Simulation (Water)	% Error
0.0	21.5	21.5	0.0	20.8	20.8	0.0
0.2	24.2	28.0	16.0	21.4	22.6	5.8
0.4	25.3	34.2	35.4	21.8	24.2	10.9
0.6	26.3	40.5	54.0	22.1	25.7	16.2
0.8	28.1	46.7	66.2	22.7	27.2	19.6

Table 3.4 : The battery surface temperature using air and water as the cooling material at 2C current rate

DoD at 2C	Experiment (Air)	Simulation (Air)	% Error	Experiment (Water)	Simulation (Water)	% Error
0.0	21.1	21.1	0.0	21.3	21.3	0.0
0.2	26.6	30.0	12.8	22.4	24.2	8.3
0.4	30.7	38.3	24.8	23.1	26.3	13.6
0.6	33.8	46.6	37.9	24.0	28.3	17.9

0.8	39.1	54.9	40.2	25.3	30.3	19.8

Table 3.5: The battery surface temperature using air and water as the cooling material at 3C current rate

DoD at 3C	Experiment (Air)	Simulation (Air)	% Error	Experiment (Water)	Simulation (Water)	% Error
0.0	20.5	20.5	0.0	19.8	19.8	0.0
0.2	28.1	31.3	11.6	21.5	23.6	9.6
0.4	33.8	41.1	21.6	22.8	26.1	14.5
0.6	38.5	50.8	32.0	24.1	28.5	18.0
0.8	43.1	62.5	45.0	26.2	30.9	17.9

From tables 3,3, 3.4, and 3.5 it can be seen that the model over predicts the battery surface temperature by an average of 19.1% and 50.5% using water and air as the cooling materials respectively. The increase in surface temperature was then obtained for each current rate and DoD, which was then compared with the experimental results as shown in Fig. 3.9(a) and (b). As seen in Fig. 3.9, the model overestimates the temperature increase at each current rate because of the losses occurring during the experimental measurements at such high currents. There is an average overestimation of the surface temperature increase by 141% and 152.1% in case with the water, and the air as the cooling material respectively.

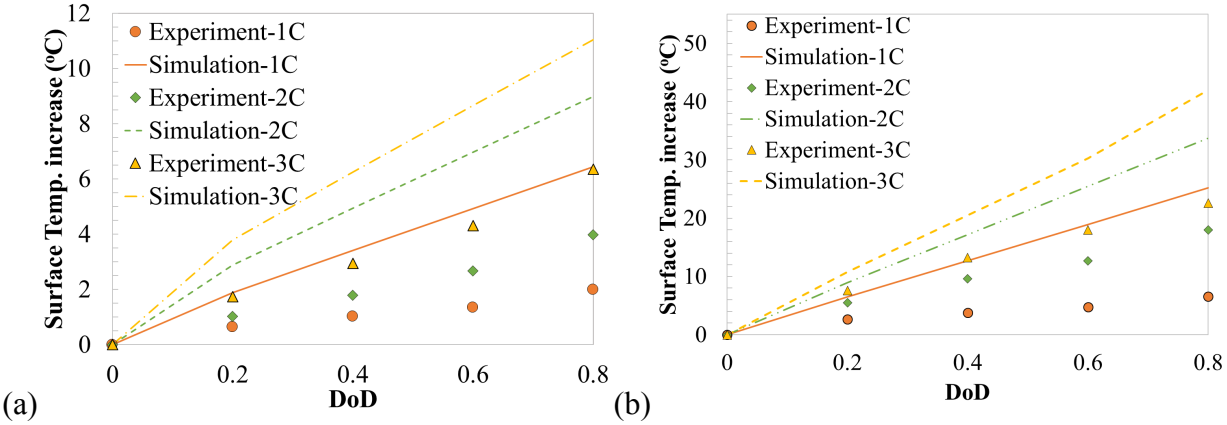

Figure 3.9: Comparison between the temperature increase obtained by experiments and simulation at various current rates using (a) water and (b) air as the cooling material.

The heat generated from 0.0 to 0.8 DoD at different current rates using simulation results were evaluated using eq (3.16).

$$q = \int_0^L \rho \cdot A \cdot c_p \cdot \Delta T \cdot dx \tag{3.16}$$

Where ΔT is the change in temperature (K) and A is the area of the battery (m^2). The validation of the thermal model is discsussed in the Appendix. Fig. 3.10 shows the comparison between the total heat generated obtained by the simulation with the experimental results using the temperature increase approach and the overpotential (OCV) [21].

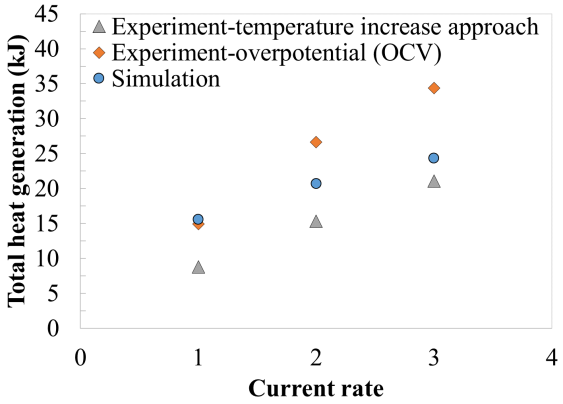

Figure 3.10: Comparison of experimental and simulated total amount of heat generation.

The values of the heat generation obtained by all three approaches and the percentage difference between them are listed in Table 3.6. Experimental result using the temperature increase and the experimental result using overpotential are labeled in the table as Expt. 1 and Expt. 2 respectively.

Table 3.6: Estimated total heat generation values using simulation and experiments

Current rate (C-rate)	Expt. 1 (kJ)	Expt. 2 (kJ)	Simulation (kJ)	% error (simulation and Expt. 1)	% error (simulation and Expt. 2)
1	14.9	8.8	15.6	4.4	43.5
2	26.7	15.3	20.7	22.4	25.9
3	34.4	21.1	24.3	29.2	13.4

We can see that the heat generation predicted by the simulation are always higher than the heat generation estimated by the temperature increase method in the experiment. Based on our experiments, an average of 33.6% of the heat generation estimated by the temperature increase approach during the experiment is actually lost to the surrounding materials through the experimental setup itself. Most of this losses are accounted for by considering the temperature increase of the hosting frame, and insulation material around the battery. The heat loss to the

surrounding material increases with the increase of the applied current. Since, we have tried to incorporate the effect of the heat losses during the experiment, we observe lesser difference in total heat generation prediction by the model and the experimental setup at 2C and 3C current rates than at 1C current rate despite 141% over prediction of the surface temperature increase.

Finally, when we compare the heat generation predicted by the model to the value estimated by the experiment using the overpotential method, only 4.4% different in the heat generation estimate at 1C current rate and a 22.4% and 29.2% at 2C and 3C current rate were observed respectively. This increase in the percentage difference in the heat generation using the model prediction and the experimental estimation using the overpotential approach may be related to the instability of the voltage at higher current rates. At higher current rates, though we measure quick increase in the battery voltage, the full capacity of the battery is never reached because of the slower chemical reactions occurring inside the battery. Thus, the measured battery voltage at such high current rates is not stable and we can observe a quick voltage drop in the battery. This might be the reason for the higher estimation of heat generation at higher current rates using overpotential method than the model heat generation estimates.

3.6 Conclusion

Electrochemical properties and heat generation characteristics of the lithium-ion battery along with the heat generation characteristic of the battery were studied. The electrolyte concentration gradient inside the battery increased with the increase of the current rate. Similarly, the overpotential increases with the increase of the current rate. The heat generation in the battery is contributed by the overpotential and the internal resistance of the battery. It was observed that the internal resistance contributed to 12.4% of the total heat generation. The simulated temperature increase is 141% and 152.1% higher than the experimental measurement to accsount for the losses that occurs during the experimental study. The total heat generation predicted by the simulation on average is 27.6% higher than the heat generation estimation by the experiments using the temperature increase approach after accounting for the experimental losses.

Nomenclature:

Acronyms:

SoC	State of Charge
DoD	Depth of Discharge
OCV	Open Circuit Voltage

Variables

A	Area
a	Specific area
Brugg	Bruggman coefficient
C	Concentration
c_p	Specific heat capacity
D	Difffusion coefficient
dx	Node size
F	Faraday's constant
I	Current
j	Current density
j_o	Exchange current density
k	Thermal conductivity
L	Battery thickness
m	Mass
$\dot{q_\eta}$	Heat generation rate due to overpotential
$\dot{q_\Omega}$	Heat generation rate due to contact resistance
$\dot{q}$	Total heat generation rate
R	Universal gas constant
R_{int}	Internal resistance
R_{sp}	Radius of the spherical particle
t	Time
t_+^0	Transference number
T	Temperature
U	Open circuit potential
x	Length from 0 to a particular point

α	Charge transfer coefficient
η	Overpotential
ε	Porosity
ρ	Density

Subscript

a	Anode
c	Cathode
e	Electrolyte phase
s	Solid phase
0	Initial value

Superscript

eff	Effective

Appendix

Solution method:

An example of the solution method followed to develop the MATLAB code in order to solve the presented model is presented below with the help of an example shown in Fig. A1 and eq (A1).

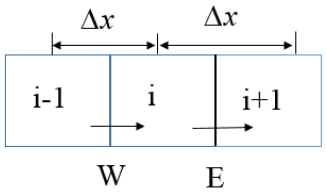

Figure A1: Discretized internal nodes.

$$\frac{\partial \Psi}{\partial t} = \alpha \frac{\partial^2 \Psi}{\partial x^2} + s \tag{A1}$$

Where Ψ represents the variable being evaluated and α can be any material property such as conductivity, density etc. The integral form of the equation is discretized using the finite volume method is given by:

$$\int_0^t \int \frac{\partial \Psi}{\partial t}\, dV\, dt = \int_0^t \int \frac{\partial^2 \Psi}{\partial x^2}\, dV\, dt + \int_0^t \int s\, dV\, dt \tag{A2}$$

The final discretized equation is represented by:

$$\frac{\Delta \Psi}{\Delta t} \Delta V = \alpha \left[-\left(\frac{\Delta \Psi}{\Delta x}\right)_{\mathrm{W}} + \left(\frac{\Delta \Psi}{\Delta x}\right)_{\mathrm{E}} \right] A_{\mathrm{x}} + s\, \Delta V \tag{A3}$$

Where subscript ‘W' and ‘E' represents the west and east boundaries respectively. $\Delta\psi / \Delta x$ is the flux passing through the boundaries and their direction at respective boundaries is shown in the Fig. A1 with an arrow. Due to their direction of flux transmission with respect to the area of the boundary, the flux at the west boundary is negative. Δt is the time step. A_x is the area perpendicular to the flux given by ($\Delta x \cdot \Delta y$). ΔV is the volume given by ($\Delta x \cdot \Delta y \cdot \Delta z$). Δx, Δy, and Δz is the length of the nodes in x, y, and z direction respectively. In our case, Δy and Δz are considered to be 1 since the model is one dimensional. The rate of accumulation of field variable within the control volume can be represented as:

$$\frac{\left(\Psi_{\mathrm{i}}^{\mathrm{n}} - \Psi_{\mathrm{i}}^{\mathrm{n-1}}\right) \Delta V}{\Delta t} \tag{A5}$$

Where superscript 'n' represents the value of the variable at current time step and superscript 'n-1' represents the value of the variable at previous time step. The flux crossing the boundaries is given by:

$$\alpha\left(-\frac{\Psi_{i}-\Psi_{i-1}}{\Delta x}+\frac{\Psi_{i+1}-\Psi_{i}}{\Delta x}\right)A_x \tag{A6}$$

Hence, the final discretized equation using the finite volume method for each cell is

$$\frac{(\Psi_{i}^{n}-\Psi_{i}^{n-1})\,\Delta V}{\Delta t}=\alpha\left(-\frac{\Psi_{i}-\Psi_{i-1}}{\Delta x}+\frac{\Psi_{i+1}-\Psi_{i}}{\Delta x}\right)A_x+s\,\Delta V \tag{A7}$$

The value of the variable α might be different for each battery component. Assuming α_i and α_{i+1} are the values of α at the nodes 'i' and 'i+1' respectively as shown in Fig. A2, we have to adjust the value of α at the interface between the two components while discretizing the governing equation.

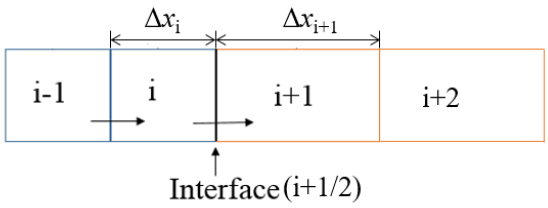

Figure A2: Discretized node with different property.

Using flux matching, i.e. the flux passing through the right and left boundary equals each other, we can evaluate α at the interface, α_{12} as

$$\alpha_{i+1/2}=\frac{\alpha_i\alpha_{i+1}\left(\frac{\Delta x_i+\Delta x_{i+1}}{2}\right)}{\frac{\alpha_1(\Delta x_{i+1})}{2}+\frac{\alpha_2(\Delta x_i)}{2}} \tag{A8}$$

Where Δx_i and Δx_{i+1} are the lengths of the nodes 'i' and 'i+1' respectively. Hence, the discretized equation at the interface with non-uniform grid at node 2 to the left of the interface is given by

$$\frac{(\Psi_{i}^{n}-\Psi_{i}^{n-1})\,\Delta V}{\Delta t}=\left(-\alpha_i\left(\frac{\Psi_i-\Psi_{i-1}}{\Delta x_i}\right)+2\alpha_{i+1/2}\left(\frac{\Psi_{i+1}-\Psi_i}{\Delta x_i+\Delta x_{i+1}}\right)\right)A_x+s\,\Delta \tag{A9}$$

Hence, the discretized equation at the interface with non-uniform grid at the node 3 to the right of the interface is given by

$$\frac{(\Psi_{i+1}^{n}-\Psi_{i+1}^{n-1})\,\Delta V}{\Delta t}=\left(-2\alpha_{i+1/2}\left(\frac{\Psi_{i+1}-\Psi_i}{\Delta x_i+\Delta x_{i+1}}\right)+\alpha_{i+1}\left(\frac{\Psi_{i+2}-\Psi_{i+1}}{\Delta x_{i+1s}}\right)\right)A_x+s\,\Delta V \tag{A10}$$

Parameter estimation:

The exchange current density for the battery was estimated by equating the overpotential at 1C current rate using experimental calculation with our model result. In the model, the anode and cathode exchange current density of 0.5 A/m^2 and 0.05 A/m^2 were determined by an iterative process to get the total overpotetial in the anode and cathode equal to 2.5V at 1C current rate, which is the average overpotential value obtained by the experiment at 1C current rate.

Then, in order to find the effective diffusion coefficient for our battery, the electrolytic concentration gradient obtained by the simulation was matched with ref [23] for the 20s discharge process using 30A current using an iterative process. The electrolyte concentration in the battery using different diffusion coefficients are shown in Fig. A3.

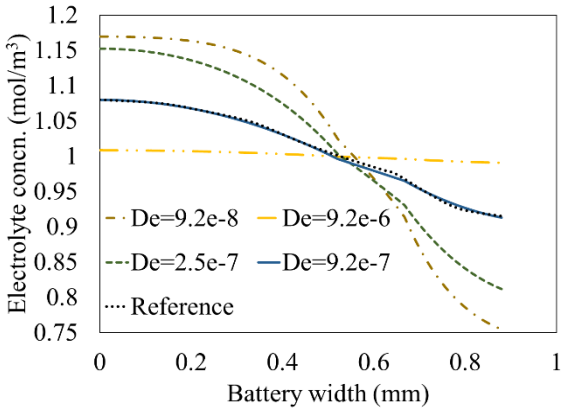

Figure A3: Comparison of simulated and reported value of electrolyte concentration using 30A discharge current for 20s.

As seen in Fig. A3, the diffusion coefficient of 9.2×10^{-7} m^2/s best fit with the reported result. With % difference of less than 0.2% difference at each point between the reported and the simulated curve shown in Fig. A3.

Model validation:

After finalizing the exchange current density and the diffusion coefficient, several simulations were run to validate the model using different node numbers to check for grid independence. In addition to that, the model was also validated by comparing the solutions obtained using different time steps and tolerance values between two consecutive iterations. Fig. 4 compares the electrolyte concentration along the battery width using various number of nodes.

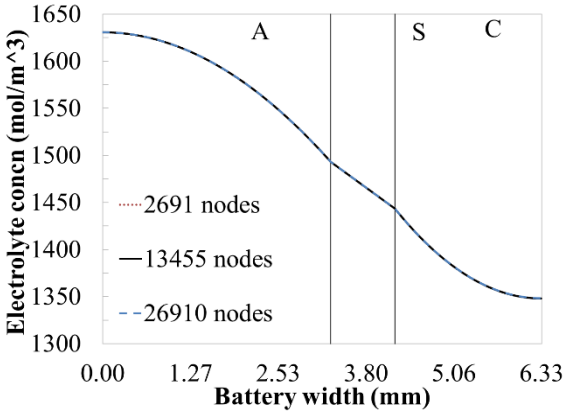

Figure A4: Comparison of the electrolyte concentration at 0.8 DoD using 3C current rate using various number of nodes.

In Fig. A4, the electrolyte concentration with 2691 (dx = 8.26×10^{-6} m), 13455 (dx = 1.65×10^{-6} m), and 26910 (dx = 8.26×10^{-7} m) nodes in the entire modeling domain are compared. Less than 0.02% difference was observed between the electrolyte concentration distribution obtained using 2691 nodes and 26910 nodes. Fig. A5 (a) and (b) compares the electrolyte concentration along the battery width using different time steps and different tolerance values respectively.

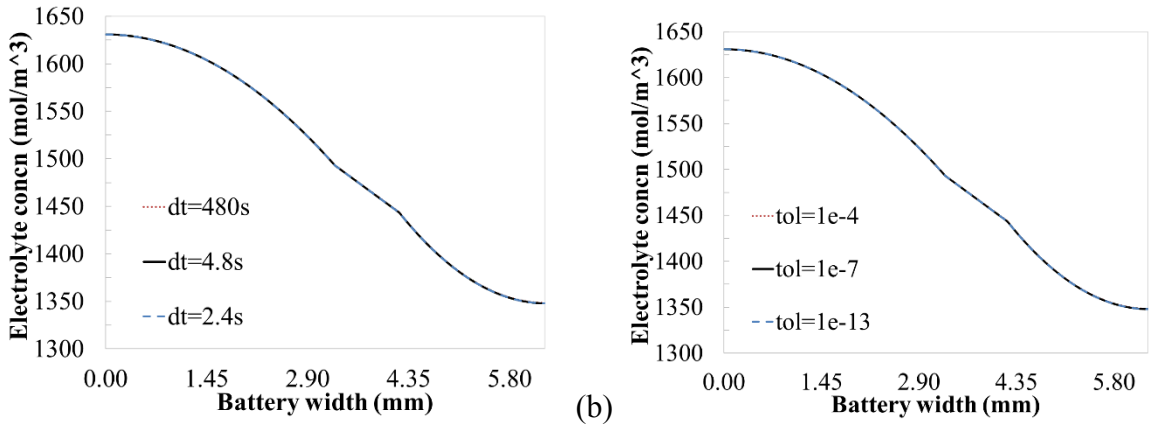

Figure A5: Comparison of electrolyte concentration at 0.8 DoD using 3C current rate along the battery using (a) different time steps (b) using different tolerance values.

The maximum difference of 0.2% was observed between the electrolyte concentration obtained using various time steps and no difference was obtained in the electrolyte concentration value using various tolerances other than the longer computation time required to complete the simulation.

Finally, in order to validate the thermal model, the heat generated obtained using air and water as the cooling material obtained from eq. (3.24) was compared with the total heat

generated obtained using the overpotential and contact resistance value. We can see in Fig. A6 that, the heat generation rate obtained using each method is equal to each other.

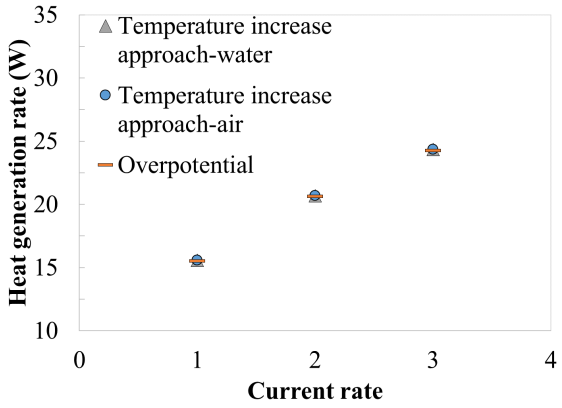

Figure A6: Comparison between the heat generation rate obtained using overpotential and contact resistance with the temperature increase method using air and water as the cooling material.

As seen is Fig. A6, the heat generation rate by the battery increases linearly with the increase in current rate. In addition to that, the total heat generated by the overpotential, temperature increase method with air and temperature increase method with water are all equal to each other. Thus, proving the validity of the results obtained by solving the thermal model.

References:

[1] T. M. Bandhauer, S. Garimella, T. F. Fuller, A Critical Review of Thermal Issues in Lithium-Ion Batteries, Journal of The Electrochemical Society, 158(2011) R1-R25

[2] W.B. Gu, C.Y. Wang, Thermal-Electrochemical Coupled Modeling of Lithium-Ion Cell, Gate Center for Advanced Energy Storage.

[3] W. Waag, C. Fleischer, D. U. Sauer, Critical review of the methods for monitoring of lithium-ion batteries in electric and hybrid vehicles, Journal of Power Sources. 258 (2014) 321-339.

[4] L. Song, J.W. Evans, Electrochemical-Thermal Model of Lithium Polymer Batteries, Journal of The Electrochemical Society. 147 (2000) 2086-2095.

[5] K.A. Smith, C.D. Rahn, C. Wang, Control oriented 1D electrochemical model of lithium ion battery, Energy Conversion and Management. 48 (2007) 2565-2578.

[6] Y. Ye, Y. Shi, N. Cai, J. Lee, X. He, Electro-Thermal modeling and experimental validation for lithium ion battery, Journal of Power Sources. 199 (2012) 227-238.

[7] M. Guo, G. Sikha, R.E. White, Single-Particle Model for a Lithium-Ion Cell: Thermal Behavior, Journal of The Electrochemical Society. 158 (2011) A122-A132

[8] X. Zhang, Thermal analysis of a cylindrical lithium-ion battery, Electrochimica Acta. 56 (2011) 12246-1255.

[9] Q. Huang, Mss. Yan, Z. Jiang, Thermal study on single electrodes in lithium-ion battery, Journal of Power Sources. 156 (2006) 542-546.

[10] B. Wu, V. Yufit, M. Marinescu, G. J. Offer, R.F. Martinez-Botas, N.P. Brandon, Coupled thermal-electrochemical modelling of uneven heat generation in lithium-ion battery packs, Journal of Power Sources. 243 (2013) 544-554.

[11] T. Dao, C. P. Vyasarayani, J. McPhee, Simplification and order reduction of lithium-ion battery model based on porous-electrode theory, Journal of Power Sources. 198(2012) 329-337.

[12] L. Cai, R.E. White, Mathematical modeling of a lithium ion battery with thermal effects in COMSOL Inc. Multiphysics (MP) software, Journal of Power Sources. 196 (2011) 5985-5989.

[13] E. Prada, D.D Domenico, Y. Creff, J. Bernard, V. Sauvant-Moynot, F. Huet, Simplified Electrochemical and Thermal Model of LiFePO4-Graphite Li-Ion Batteries for Fast Charge Applications, Journal of The Electrochemical Society. 159 (2012) A1508-A1519.

[14] E. Prada, D.D. Domenico, Y. Creff, J. Bernard, V. Sauvant-Moynot, F. Huet, A Simplified Electrochemical and Thermal Aging Model of LiFePO4-Graphite Li-ion Batteries: Power and Capacity Fade Simulations, Journal of The Electrochemical Society. 160 (2013) A616-A628.

[15] K. Smith, C. Wang, Power and thermal characterization of lithium-ion battery pack for hybrid-electric vehicles, Journal of Power Sources. 160 (2006) 662-673.

[16] P.W.C. Northrop, V. Ramadesigan, S. De, V.R. Subramanian, Coordinate Transformation, Orthogonal Collocation, Model Reformulation and Simulation of Electrochemical-Thermal Behavior of Lithium-Ion Battery Stacks, Journal of The Electrochemical Society. 158 (2011) A1461-1477.

[17] R. Klein, N. A. Chaturvedi, J. Christensen, J. Ahmed, R. Findeisen, A. Kojic, State estimation of a reduced electrochemical model of a lithium-ion battery, American Control Conference. (2010) 6618-6623.

[18] M. Xu, Z, Zhang, X. Wang, L. Jia, L. Yang, Two-dimensional electrochemical-thermal coupled modeling of cylindrical LiFePO4 batteries, Journal of Power Sources. 256 (2014) 233-243.

[19] M. Xu, Z. Zhang, X. Wang, L. Jia, L. Yang, A pseudo three-dimensional electrochemical-thermal model of a prismatic LiFePO4 battery during discharge process, Energy. 80 (2015) 303-317.

[20] W. Fang, O. J. Kwon, C. Wang, Electrochemical –thermal modeling of automotive Li-ion batteries and experimental validation using a three-electrode cell, International Journal of Energy Research. 34 (2010) 107-115.

[21] S. Neupane, M. Alipanah, X. Li, Heat generation characteristics of lithium ion batteries with passive thermal management, International Journal of Heat and Mass Transfer (under-review).

4. Future work

The experimental and model study presented in this thesis can be further explored. Many such adaptations have been left for the future work due to the lack of time. Future work concerns the deeper analysis of battery behavior and new proposals to try different methods, and curiosity to learn more. The following experiments can be carried out:

- The experimental study can be conducted for pulsed charging-discharging cycles up to higher current rates such as 10C in order to study the heat generation characteristic of the battery in actual driving conditions.
- The temperature testing can also be further done using other various composite cooling materials such as Al foam + PCM, and also by incorporating nano-materials to the cooling material. It can be an interesting study on the thermal management of the battery to further explore and find other alternative materials for passive cooling.
- In addition to that, study of the change in the internal resistance of the battery along with the heat generation characteristics during the charge-discharge cycle can be done. It can provide better insight on the effect of thermal management on the internal resistance that directly affects the battery performance and the battery life.

In addition, the simplified model presented in this work can be further modified and developed to explore larger breadth and depth of lithium ion battery characteristics. Some of the suggested works include:

- Modifying the model to simulate the battery characteristic during the charging process. The charging model, when incorporated into the discharging model presented in this work, can help us better understand the electrochemical and thermal properties of the battery during a charge-discharge cycle as conducted in our experimental study. It can also be used for studying the behavior of a battery pack.
- Creating a simplified model capable of simulating the battery performance using pulsed current can be very useful for the study of battery behavior. Such model can be used to simulate actual driving conditions and understand the real-time electrochemical and thermal behaviors of batteries.